



ISSN 1028-8546

Volume XXIII, Number 1

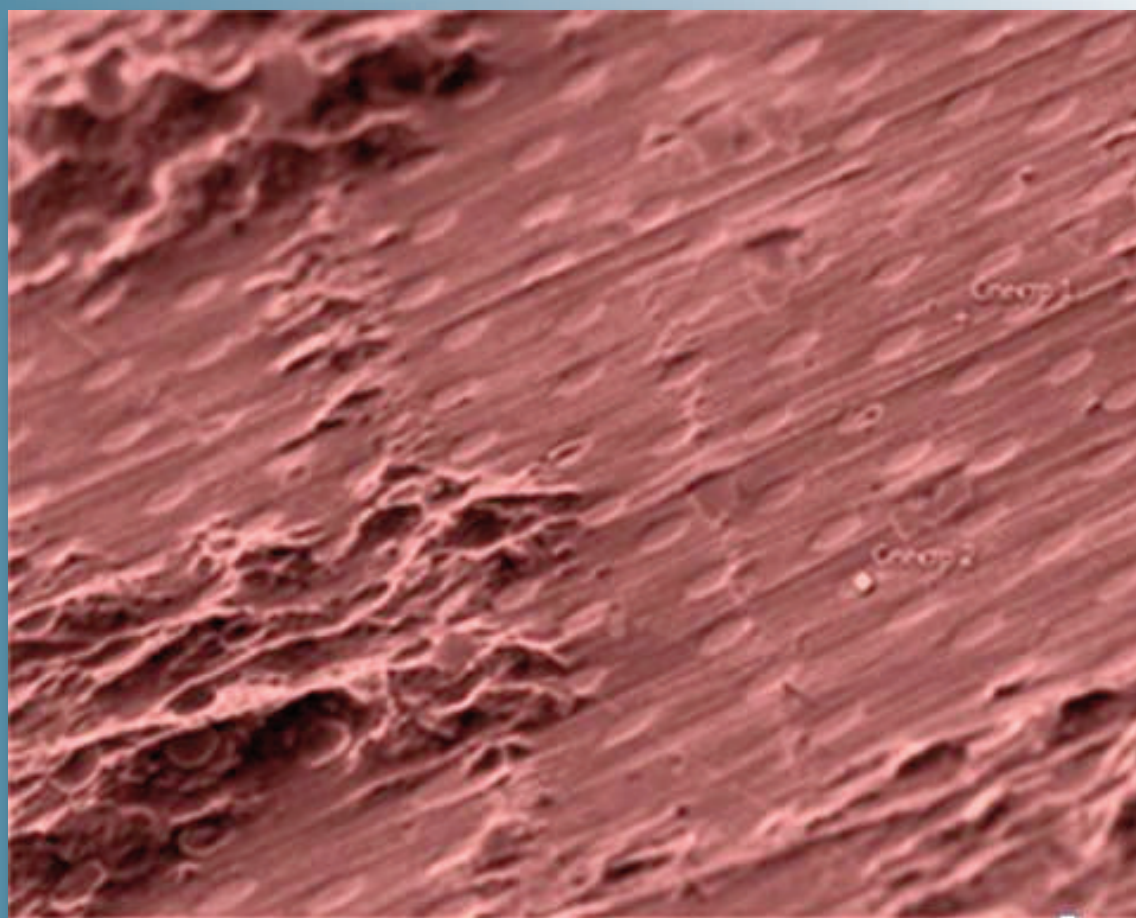
Section: En

April, 2017

Azerbaijan Journal of Physics

Fizika

www.physics.gov.az



G.M. Abdullayev Institute of Physics
Azerbaijan National Academy of Sciences
Department of Physical, Mathematical and Technical Sciences

Azerbaijan Journal of Physics

FIZIKA

*G.M.Abdullayev Institute of Physics
Azerbaijan National Academy of Sciences
Department of Physical, Mathematical and Technical Sciences*

HONORARY EDITORS

Arif PASHAYEV

EDITORS-IN-CHIEF

Nazim MAMEDOV

Chingiz QAJAR

SENIOR EDITOR

Talat MEHDIYEV

INTERNATIONAL REVIEW BOARD

Ivan Scherbakov, Russia
Kerim Allahverdiyev, Azerbaijan
Mehmet Öndr Yetiş, Turkey
Gennadii Jablonskii, Buelorussia
Rafael Imamov, Russia
Vladimir Man'ko, Russia
Eldar Salayev, Azerbaijan
Dieter Hochheimer, USA
Victor L'vov, Israel
Vyacheslav Tuzlukov, South Korea

Majid Ebrahim-Zadeh, Spain
Firudin Hashimzadeh, Azerbaijan
Anatoly Boreysho, Russia
Mikhail Khalin, Russia
Hasan Bidadi, Tebriz, Iran
Natiq Atakishiyev, Mexico
Tayar Djafarov, Azerbaijan
Arif Hashimov, Azerbaijan
Javad Abidinov, Azerbaijan
Bagadur Tagiyev, Azerbaijan

Talat Mehdiyev, Azerbaijan
Vali Huseynov, Azerbaijan
Ayaz Baramov, Azerbaijan
Tofiq Mammadov, Azerbaijan
Salima Mehdiyeva, Azerbaijan
Shakir Nagiyev, Azerbaijan
Rauf Guseynov, Azerbaijan
Almuk Abbasov, Azerbaijan
Yusif Asadov, Azerbaijan

TECHNICAL EDITORIAL BOARD

Senior secretary Elmira Akhundova, Nazli Guseynova, Sakina Aliyeva,
Nigar Akhundova, Elshana Aleskerova, Rena Nayimbayeva

PUBLISHING OFFICE

131 H.Javid ave, AZ-1143, Baku
ANAS, G.M.Abdullayev Institute of Physics

Tel.: (99412) 539-51-63, 539-32-23
Fax: (99412) 447-04-56
E-mail: jophphysics@gmail.com
Internet: www.physics.gov.az

It is authorized for printing:

Published at "SƏRQ-QƏRB"
17 Ashug Alessger str., Baku
Typographer : Aziz Gulaliyev

Sent for printing on: __.__. 201_
Printing approved on: __.__. 201_
Physical binding: _____
Number of copies: _____ 200
Order: _____

GAS DISCHARGE DEVICE BASED ON THE POROUS ZEOLITE MICROSTRUCTURE

I.C. KOÇUM³, U. BUNYATOVA³, B.G. SALAMOV^{1,2*} AND M.M. SHIRINOV²¹Physics Department, Faculty of Sciences, Gazi University,
Beşevler 06500 Ankara, Turkey²National Academy of Science, Institute of Physics, AZ-1143 Baku, Azerbaijan³Department of Biomedical Engineering, Faculty of Engineering,
Baskent University, Baglica, Ankara, Turkey

* bala@gazi.edu.tr

The stabilization of glow microdischarges in a *dc* air cold plasma is studied experimentally functions of pressure p (18-760 Torr) and interelectrode distances d (50-250 μm) in the gas discharge electronic device (*GDED*) with nanoporous zeolite cathode modified by Ag nanoparticles (resistivity $\sim 10^{11}$ - $10^6 \Omega\cdot\text{cm}$). Comparison of current and discharge light emission (*DLE*) from glow microdischarges are used for the determination of the stabilization under low- and atmospheric pressure conditions. It is found that the gas *DLE* inside the nanoporous zeolites develop from the surface if the amplitude of the applied voltage reaches given threshold. Moreover, uniform *DLE* can be generated in air up to atmosphere pressure. It is also shown that breakdown voltage U_B is reduced significantly at atmospheric pressure when zeolite cathode modified by Ag nanoparticles is used. Due to the very small electrode gap width we can describe the behaviour of the charged particles in the electric field of our system with the *dc* Townsend breakdown theory, depending on the pressure range. The generation and maintenance of stable cold plasma is studied according to the effect of Ag nanoparticles.

Keywords: nanoparticles, atmospheric pressure plasma, conductivity mechanisms, electrical properties, nanoporous zeolite**PACS:** 52.25.Jm; 52.80.-s; 51.50.+v

1. INTRODUCTION

There is growing interest in non-thermal plasma processing techniques optimized for atmospheric pressure applications due to their significant industrial advantages. At atmospheric pressure, thin film deposition at very high rates is possible, and cost-intensive vacuum technology can be avoided. Many approaches have been proposed in the last 15 years to overcome the problems of generating and sustaining a stable, uniform and homogeneous non-thermal atmospheric pressure (*AP*) plasma [1,2].

In spite of intensive research in the field of metal nanoparticles (NPs) and clusters, the problem of proper size-control and materials fabrication with particles of the desired properties still exists, because each type of material requires new approach for the development of appropriate synthesis conditions of clusters and NPs [3]. In that sense, the physico-chemical interaction between plasma and the loaded active metals, such as silver NPs [4] is still not well understood. For that purpose, using nanoporous materials, such as zeolites, modified with active metal NPs can be an alternative to clarify the possibilities of using these materials in practical plasma applications. Considering availability of strong effect of metal NPs and especially silver on discharge plasma of gas discharge electronic device (*GDED*), further experimental studies are needed to provide insight into the physico-chemical processes influencing the plasma characteristics and cathode properties.

Operating efficiently of the system will be based on the use of zeolite cathode (*ZC*), which is a good absorber of gas molecules in their nanoporous. The electrode dimensions, especially the electrode gap width d in the micrometer range, are small enough to generate sufficiently high electric field strengths to ignite *AP* glow

discharges applying *dc* voltages (less than 1.5 kV). With this last type of *GDED* plasma can be generated in air at *AP*. For these reasons, it is important to know the relation between the geometrical parameters and the discharge characteristics from the viewpoint of the cell optimization.

Deliberate modification of electrode surfaces with zeolites has evoked considerable interest. The attractive zeolite characteristics that are liable to affect the electron transfer reactions at an electrode-discharge interphase are (a) the size and shape selectivity due to the rigid structure made of pores and channels of molecular dimensions; (b) the cation-exchange capacity arising from the charge compensation of the negatively charged aluminosilicate lattice by mobile extra framework cations; and (c) the catalytic properties of both intrinsic and extrinsic sites of the microporous materials. This has led to the design, preparation, and use of various zeolite-modified electrodes.

The zeolite frameworks are formed by chains of *Si* and *Al* anionites. The framework has a negative charge because of its structure and this charge is compensated by water molecules and cations of alkali and alkali-earth metals Ca, K, Na, Mg weakly connected with it. Water can be removed by heating or evacuation of the zeolite, which has no effect on a rigid framework, its structure is virtually unchanged. The zeolite pores have the right forms. Connecting between each other through "windows" (0.26-0.27 nm), they form the perforated channel chain. That's why the zeolites can be considered as the object on which besides well-known phenomena (adsorption, ion-exchange phenomena), investigate the electron porous emission, electron multiplication and gas discharge in pores, dielectric and electric properties at pore saturation by different gases and liquids. Consequently, the peculiarities of plasma generation in

the GDED system with Ag-modified metal nanoparticles in this study we investigate the enhanced efficiency of Ag⁰-ZC on the fundamental characteristics of GDED. Besides operation at AP, in this study we showed that Ag⁰-ZC is an effective material for reducing the breakdown voltage (U_B) substantially and charge transport occurs at lower voltages with respect to un-modified ZC.

2. EXPERIMENTAL

The behaviour of the current-voltage characteristic (CVC) of the discharge cell with ZC is determined by the type of the discharge. Therefore CVCs of the ZC plate were taken at different residual pressures and the GDLE from the pores was simultaneously detected. Natural zeolite was taken as a porous object. Zeolites are non-stoichiometric compounds, the compositions of which vary over wide limits and produce a series of solid solutions. Zeolites are aqueous aluminosilicates in which an infinite aluminosilicate frame is produced by $[\text{SiO}_4]^{4-}$ and $[\text{AlO}_4]^{5-}$ tetrahedra having common vertices. These tetrahedra have communicating cavities occupied by large ions and water molecules [5]. Clinoptilolite is the most abundant of the natural zeolites [6], but composition and purity vary widely among the many deposits found throughout the world. For our study we used $(\text{Ca}, \text{K}_2, \text{Na}_2, \text{Mg})_4\text{Al}_8\text{Si}_{40}\text{O}_{96} \times 24\text{H}_2\text{O}$ the clinoptilolite from Western Turkey deposit in Gordes Manisa. This natural zeolitic material contains on average 90-95% of the clinoptilolite zeolitic mineral [7,8]. Clinoptilolite belongs to a class of zeolite minerals having the clear-cut structural topology of heulandite (HEU) and the ratio of Si/Al > 4.0. The structural topology of the HEU tetrahedral lattice is well understood. At the same time, Fig. 1 shows the SEM-EDX analyses composition of ZC and Ag⁰-ZC samples.

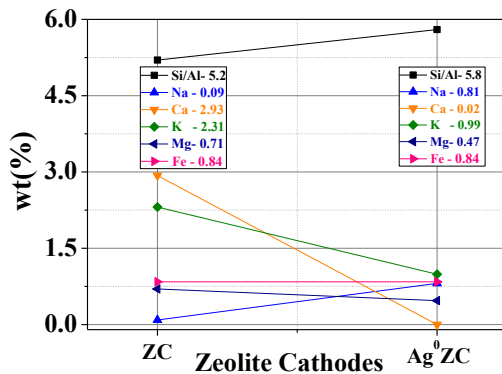


Fig. 1. The SEM-EDX determined chemical composition of un-modified and Ag⁰-ZC samples.

The experiments were carried out with natural ZC and silver modified Ag⁰-ZC plate ($\rho \sim 10^{11}-10^6 \Omega \cdot \text{cm}$) [9]. The ZC used in this work is plates having a diameter D of 22 mm and a thickness of 2 mm. The pressure in the chamber was monitored by a digital manometer attached to a pumping system and was kept at a certain constant value during the whole course of measurement. The entire experimental study of this work was performed in ambient air from AP to 10^{-2} Torr pressures and the

measurements were carried out at room temperature. The setup (Fig. 2) used here is similar to that applied earlier [10,11], where a GDED with a GaAs photodetector was studied at room temperature.

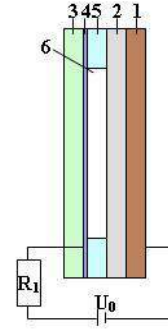


Fig. 2. Scheme of the gas discharge cell: 1- metallic contact; 2- zeolite plate; 3- flat glass disk; 4- semi-transparent conductive SnO₂ contact; 5- insulating mica sheet; 6- gas discharge gap.

3. RESULTS AND DISCUSSION

I-V characteristics of a GDED with ZC and Ag⁰-ZC for different pressures were investigated. Fig. 3 gives typical I-V characteristics for the discharge cell with different gap distances d (50-250 μm) of the ZC. Due to the very small d we can describe the behaviour of the charged particles in the electric field of GDED with the dc Townsend breakdown theory, depending on the pressure range. At this point, we assume that a *homogeneous stationary* Townsend discharge [12] is established in the GDED. From the physical point of view, the most important feature of this kind of gas discharge is that space charge effects inside the gap are small and do not cause a distortion in the electric field between the electrodes. Another characteristic property is the homogeneous distribution of the current density perpendicular to the current flow. The DLE from the discharge is also homogeneous, while the wavelength of the DLE depends on the filled gas. The DLE intensity is proportional to discharge current. A local change of a ZC resistance leads to a local change of the current and the DLE [13].

Hence, the principle of operation of the GDED is based on some specific properties of the Townsend discharge. The voltage drop at the discharge gap for Townsend discharge mode is independent of the current. Therefore, the slope of the I-V characteristics provides the resistance of the ZC. Then, the specific conductivity can be computed from the resistance and the geometric dimensions. We notice that the current density in the GDED in the investigated parameter range does not exceed the limiting current for the existence of the Townsend discharge at given experimental conditions [14]. We remark that the feeding voltage V_0 is the sum of the voltage drops at the gas gap and at the zeolite component. One of the characteristic features of the Townsend discharge is the constancy of the voltage drop V_B at the discharge domain while current varies.

The range of the stationary operation and current depends on type of the ZC and interelectrode distances d [15]. Considering this figure for the GDED with a ZC and Ag⁰-ZC one can note the following: (a) the increment of

pressure leads to a increase in U_B values for air (i.e. at 44 Torr $U_B = 365$ V for ZC and $U_B = 345$ V for Ag^0 -ZC); (b) the current and U_B values rise abruptly at AP (i.e. at 760 Torr $U_B = 710$ V for ZC and $U_B = 380$ V for Ag^0 -ZC); (c) the high current values were obtained at lower voltages for Ag^0 -ZC compared to ZC electrodes. The slope of Ag^0 -ZC is higher with respect to un-modified ZC for a wide pressure range, which suggests that Ag modification (Ag^0 -ZC) leads to enhanced conductivity with respect to ZC.

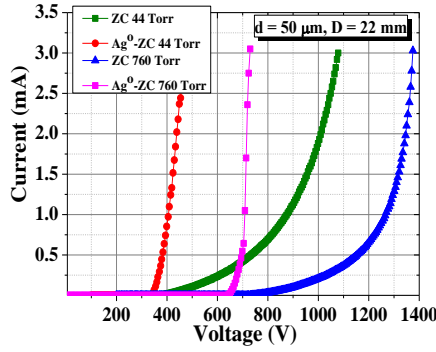


Fig. 3. I-V characteristics of a GDED with respect to pressure for ZC and for Ag^0 -ZC.

It can be seen that the I-V characteristics have a smooth current increase, but they are completely different from the same characteristics of the GDED with GaAs semiconductor cathode (for comparison see Fig. 2 in [16]). Fig. 3 also show that with a change in type of ZC the U_B changes and the form of the I-V characteristics is reproducible, except for minor differences in the values of the current. Our previous works [17] commented on the physical properties of discharges generated inside the porous ZC by dc driven discharges. The detailed description of the discharge properties with respect to the effect of the pore size, discharge power, and gas mixture can be found in [18]. The results showed that the microplasmas inside the ceramic foam formed only for the specific discharge power and pores size of the ceramics. At small voltages, a surface barrier discharge on the surface of the ceramics may only be observed. With the increase of the applied voltage, however, the surface discharges transits into capillary microdischarges inside the ceramics, which onset voltage increases with the decreasing pores size. Upon the transition to microdischarges, the amplitude of the current pulses increases extremely, as well as the corresponding discharge current and power. The increase of the discharge current is larger for the bigger pore size, due to the increase of the radius of the discharge channel and volume of the generated microplasma.

Moreover, the adsorption of water by zeolites has some peculiarities. For all types of the zeolites very sharp rise of the isotherms is observed at low concentrations of water vapor. Adsorption capacity of zeolites at ambient temperatures (T_a) and for pressure of 1 - 2 Torr is very close to the maximum saturation P_w . Moreover, even at very low pressures NaA zeolite exhibits significant adsorption capacity of water [19]. The second

distinguishing feature of the water vapor adsorption by zeolites is to maintain the adsorption capacity even at significant change of temperatures. At $T_a = 100$ °C and $P_s = 10$ Torr, the adsorption capacity X of the zeolite is 15-16 g/100 g. Moreover, approach to 200 °C the X is still significant and no less than - 4 g/100 g [20]. With increasing T_a , the difference in the adsorption capacity X of zeolites is further increased, which is a distinctive feature of adsorption on zeolites. Oscillations of gas temperature do not introduce significant changes in the X of the synthetic zeolite. However, it should be noted the following significant disadvantage. Zeolites greedily absorb humidity, but they are hard to give it during dehydration process. At the same time, according to a global model based on He/ H_2O plasma chemistry, water vapor plasmas are dominated by OH, O, and O_2 metastable species and water cluster ions depending on the concentration of water vapor in the gas [21]. An increase in water vapor concentration in the gas mixture leads to an increase in the reduced electric field strength E/N in the plasma, which results in a higher intensity of OH generations [22,23]. Water is also an important impurity in numerous AP discharges of practical interest. For example, discharges in atmospheric air typically contain water vapour in concentrations of thousands of parts per million (air at 25° and 25% relative humidity contains ~ 7750 ppm of water) [21,24].

Strictly speaking, the most suitable interelectrode distance is $d = 50$ μm up to the AP. This situation indicates that the better stabilization of dc glow discharges at AP can be obtained for ZC in GDED. Thus, it is possible to produce gas discharges up to AP by means of GDED at moderate voltages so that wide areas of plasma applications become feasible under those conditions. For further step, the physical processes determining the stable function of an ionization system and spatial stabilization of the discharge can be taken into account as a result of the distributed resistance of the ZC. Because, stabilization effect is closely related to the I-V characteristics results obtained for different gap distances d in the discharge cell. Therefore, representative plots of measured breakdown curves for the ZC and Ag^0 -ZC in cases of different gap distances d are shown in Fig. 4.

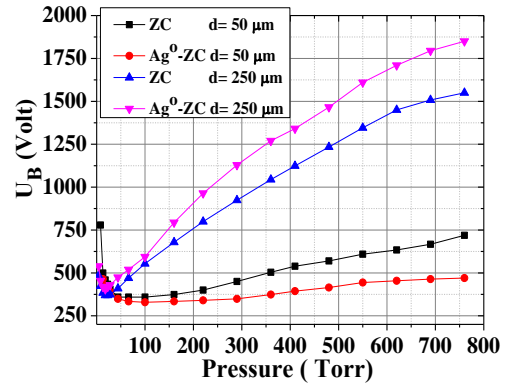


Fig. 4. Measured breakdown curves for the ZC and Ag^0 -ZC.

With a change in the residual gas pressure up to AP the current changes. In a running experiment, the pressure

p and the conductivity of the porous ZC and $\text{Ag}^0\text{-ZC}$ are fixed, and the supply voltage U_0 is slowly increased from 0 V, thereby increasing the voltage drop at the gas layer. As soon as U_0 reaches the critical voltage for breakdown in the gas, homogeneous ignition of the discharge takes place. The value of the critical voltage and residual pressure are determined by the so-called Paschen curve [25].

Inset in Fig. 5 shows detailed information regarding the I-V characteristics of the cell with respect to pressure when a dc voltage of a high enough magnitude is applied to the system. The voltage value from U_B to feeding voltage U_0 applied to the electrodes is the potential drop across the ZC, whereas the value from 0 to U_B is mainly the potential drop at the discharge gap. The optimal operation value of d is found as 50 μm for air-filled GDED. However, the atmospheric pressure is much more compatible and optimal for planar gas discharge cell with ZC, as shown in the values of current (see inset) and GDLE in Figs.5, respectively. In addition, discharge currents and GDLE intensities in GDED with $\text{Ag}^0\text{-ZC}$ at minimum feeding voltage (450 V) are much larger and intensive compared to the air-filled cell with ZC. In the GDED with ZC, GDLE satisfies the optimal and effective conditions at lower pressures (44-160 Torr), i.e., the current and DLE intensities in this media are high. However, the situation of current and GDLE intensities becomes vice versa near the AP. In other words, while an instant decrease in the GDLE intensities from the GDED with ZC is observed, higher GDLE intensities are obtained from cell with $\text{Ag}^0\text{-ZC}$, conversely. Moreover, maximum GDLE intensity values are very different in GDED with ZC, whereas these values are the almost the same in system with $\text{Ag}^0\text{-ZC}$ near the AP, as shown Fig. 5. This situation proves that one should prefer to use $\text{Ag}^0\text{-ZC}$ at APs rather than ZC since the GDLE values are considerably better. It can be also stated that the better stabilization of dc glow discharges at APs can be obtained for GDED with $\text{Ag}^0\text{-ZC}$.

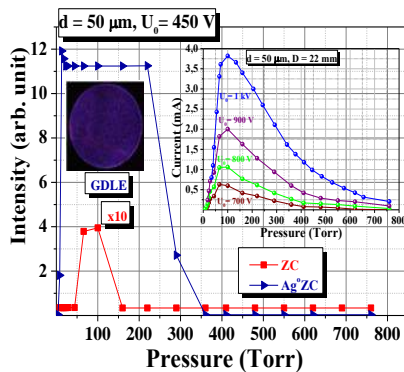


Fig. 5. GDLE dependence on pressure for GDED with ZC and $\text{Ag}^0\text{-ZC}$.

It is also found that the slopes of current curves depend on the D . GDLE inside the porous zeolites develop from the surface if the amplitude of the applied voltage reaches given threshold. Discharge inside the pores of ZC framework is produced by dc power supply and produce relatively cold microplasmas with high level

of non-equilibrium with no instabilities. It is found that the gas in ZC pores ionizes and, accordingly, the number of electrons in the pores grows. It is shown that especially $\text{Ag}^0\text{-ZC}$ in a planar gas discharge cell considerably reduces the ignition voltage of the GDED.

Fig. 5 shows the same behaviour of the GDLE in a gas discharge cell with the $\text{Ag}^0\text{-ZC}$ and ZC. For a thin discharge gap of the cell the proportionality between the gas brightness and the current density, j , can be observed in a broad range of j . Note that when the feeding voltage is higher than 400 V, the curve for $\text{Ag}^0\text{-ZC}$ in Fig.5 represents the saturation of the GDLE intensity, which is related to the maximal limit of the photomultiplier. Moreover, the shape of the I-V characteristics and the GDLE intensity in a system depend on the voltage increment of the power supply [10].

The dependence of the intensity of the GDLE and ignition of discharges associated with all nanopores of ZC on the electric field strength is shown in Fig. 5. We have observed a significant increase of the discharge brightness in the discharge gap with $\text{Ag}^0\text{-ZC}$ compared to that of the main traditional discharge gap with unmodified ZC [26]. It is seen that the gain G increases exponentially with feeding voltage. Such dependence is in accordance with the literature data for gain measurements in gas electron multipliers [27] and reflects the existence of the avalanche electron multiplication mechanism. One can see that in this case there is a significant increase in the output brightness, which takes place thanks to initiation of a self-sustained discharge in the multichannels. At fixed feeding voltage U_0 the brightness is proportional to the current density of the gap and seems to behave linearly to the current range covered here. The maximum gain achieved in the present work is 50 for the pressure of 100 Torr and the feeding voltage $U_0 = 450$ V. The filamentation was primarily due to the formation of a space charge of positive ions in the discharge gap, which changed the discharge from the Townsend to the glow type [28,29]. The intensity of GDLE in the system with $\text{Ag}^0\text{-ZC}$ exceeds the intensity of the DLE in the system with ZC.

The obtained electrical characteristics of GDED with a $\text{Ag}^0\text{-ZC}$ and the comparison of the discharge patterns show that the system possesses a noticeably larger discharge light amplification or gain G . Electrons entering the pores of the $\text{Ag}^0\text{-ZC}$ in the discharge gap are multiplied in the electric field by the avalanche mechanism, so that a rather small current in the discharge gap without pores becomes a much larger current in the gap with $\text{Ag}^0\text{-ZC}$. Since the current is concentrated in the pores of ZC, the source of the loss of resolution i.e., electron scattering with the flight between the discharge electrodes disappears [30]. Thus, the GDED with ZC and $\text{Ag}^0\text{-ZC}$ shows good technical performance. The GDLE of the latter is observed from the backside of the structure. Thus, it is experimentally demonstrated that gas discharge gap with ZC can be used for generating and sustaining a stable, uniform and homogeneous non-thermal atmospheric pressure plasma.

4. CONCLUSION

In this study, we showed that Ag-modified-zeolite is an effective material for reducing the breakdown voltage

(U_B) substantially and charge transport occurs at lower voltages with respect to un-modified zeolite. Moreover, some new results were related with the role of Ag metal NPs in the discharge characteristics, including the analysis of physical processes initiating the electrical breakdown and spatial stabilization of the current in order to enhance electro-chemical/ electron-transfer processes and maintenance of stable discharges up to AP.

By analysing the current and optical emission from a plasma discharge, more complete information can be obtained about the possibility of varying the intensity of the light emitted by a *GDLED* with ZC, especially with its working as plasma light source with the prolonged working time. Specific geometry of the zeolite channels structure and the strong electric field in the nanopores provide an efficient electron multiplication and related excitation of gas atoms. The use of gas discharge gap with nanoporous Ag^0 -ZC leads to increase in the *GDLE* intensity. In a system with Ag^0 -ZC, the total intensity of *GDLE* exceeds the intensity of uniform *GDLE* in the *GDLED* with ZC. This device may find an application in

for generating and sustaining a stable, uniform and homogeneous non-thermal atmospheric pressure plasma.

Thus, it is experimentally demonstrated that *GDLED* with Ag^0 -ZC can operate as an effective light intensifier up to AP with gain values of 40÷50 observed. We also believe that on the basis of the outlined principles, by using dielectric spacer of proper design with a large number of multi-channels and a single-hole microcapillary discharge plate (i.e. suggested in [31]) it is possible to build ultrafast and rather sensitive large emitting area plasma light source with internal image amplification.

ACKNOWLEDGMENTS

The authors thank the Turkish Scientific and Technological Research Council of Turkey (TUBITAK) for the financial support of this work through BIDEB-2221. The author wishes to acknowledge the Rota Mining Corporation, Gördes, Manisa, Turkey, for providing the clinoptilolite samples.

- [1] T. Yokoyama, M. Kogoma, T. Moriwaki and S. Okazaki. 1990 J. Phys. D: Appl. Phys. 23 1125.
- [2] F. Massines, A. Rabehi, P. Decomps, R.B. Gadri, P. Segur and C. Mayoux. 1998, J. Appl. Phys. 83 2950.
- [3] V.S. Gurin, V.P. Petranovskii, N.E. Bogdanchikova. 2002, Mater. Sci. Eng. C 19 N 1-2, 327-331.
- [4] H.-Ha Kim, J.-Ho Kim, A. Ogata. 2009, J. Phys. D: Appl. Phys., 42, N 13, 135210.
- [5] G. Gottardi and E. Galli. 1985, Natural Zeolites (Berlin: Springer).
- [6] C. Senaratne, J. Zhang, M.D. Baker, C.A. Bessel, D.R. Rolison. 1996, J. Phys. Chem. 100 5849.
- [7] A. Giaya, R.W. Thompson, R. Denkwicz. 2000, Microporous Mesoporous Mater. 40 205.
- [8] Ch. Baerlocher, W.M. Meier and D.H. Olson. 2001, Atlas of Zeolite Framework Types (Amsterdam: Elsevier).
- [9] G. Vitale, L. Bull, R.E. Morris, A.K. Cheetham, B.H. Toby, C.G. Coe and J.E. MacDougall. 1995, J. Phys. Chem. B 99 16087.
- [10] B.G. Salamov, S. Büyükkakış, M. Özer, K. Çolakoglu. 1998, Eur. Phys. J. Appl. Phys. 2 275.
- [11] V.I. Orbukh, N.N. Lebedeva, S. Ozturk, B.G. Salamov. 2013, Superlattices and Microstructures 54 16-25.
- [12] B.G. Salamov, Ş. Ellialtınoğlu, B. Akinoglu, N.N. Lebedeva. 1996, J. Phys. D: Appl. Phys. 29 628.
- [13] B.G. Salamov, K. Colakoglu and S. Altındal 1995, Infrared Phys. & Technol. 36 661.
- [14] H. Willebrand, Y. Astrov, L. Portsel, S. Teperick and T. Gauselmann. 1995, Infrared Phys&Technol. 36 809.
- [15] H.Y. Kurt and B.G. Salamov. 2003, J. Phys. D: Appl. Phys. 36 1987.
- [16] B.G. Salamov, Y. Çiftci, K. Çolakoglu. 2004, IEEE Transactions on Plasma Science 32 2093.
- [17] V.I. Orbukh, N.N. Lebedeva, S. Ozturk, S. Uğur, B.G. Salamov. 2012, J. Optoelectron. Adv. Mater. 4 205.
- [18] K. Hensel, V. Martisovits, Z. Machala, M. Janda, M. Lestinsky, P. Tardiveau, A. Mizuno. 2007, Plasma Process. Polym. 4 682-693.
- [19] A. Arbuzyanov, V. Vasilyev, A. Goursot. 1998, Surface Science, 397 395-405.
- [20] D.W. Breck. Zeolites Molecular Sieves, R.E. Krieger Pub., Malabar 1984, pp. 392-410.
- [21] D.X. Liu, P. Bruggeman, F. Iza, M.Z. Rong, M.G. Kong. 2010, Plasma Sources Sci. Technol., 19 025018.
- [22] Y.S. Akishev, A.A. Deryugin, V.B. Karalnik, I.V. Kochetov, A.P. Napartovich, N.I. Trushkin. 1994, Plasma Phys. Rep., 20 511.
- [23] A. Van Deynse, N. De Geyter, C. Leys, R. Morent. 2014, Plasma Process. Polym. 11 117-125.
- [24] R.H. Perry, D.W. Green. Perry's Chemical Engineers' Handbook, McGraw-Hill, New York 1997.
- [25] Y.P. Raizer. 1991, Gas Discharge Physics (Berlin: Springer).
- [26] K. Koseoglu, M. Özer, S. Ozturk, B. G. Salamov. 2014, Jpn. J. Appl. Phys., 53 086203.
- [27] H. Sakurai, T. Tamura, S. Gunji, and M. Noma. 1996, Nucl. Instrum. Methods Phys. Res. A 374 341.
- [28] K. Aktas, S. Acar, B.G. Salamov. 2011, Plasma Sources Sci. Technol. 20 045010.
- [29] B.G. Salamov, M. Kasap and N.N. Lebedeva. 2000, J. Phys. D: Appl. Phys. 33 2192.
- [30] A.V. Phelps, B.M. Jelenkovic. 1987, Phys. Rev. A 36 5327.
- [31] L.M. Portsel, V.M. Marchenko and H.G. Purwins. 2005, J. Appl. Phys. 97 076101.

Received: 27.03.2017

A MICROSCOPIC THEORY OF SPIN EXCITATIONS IN A CYLINDRICAL FERROMAGNETIC NANOTUBES

V.A. TANRIVERDIYEV, V.S. TAGIYEV

Institute of Physics of the National Academy of Sciences of Azerbaijan,

Baku Az -1143, Baku, H. Javid ave.33,

E-mail: Vahid_tanriverdi @yahoo.com

Spin-waves excitations in a cylindrical ferromagnetic nanotubes are investigated by use of the Green function method. The nano-tube consists of the core and the surface shell and the core is surrounded by the surface shell. The expressions of Green's function for different spins of ferromagnetic nanotubes are obtained. The temperature dependence of magnetization is clarified in the surface shell and core. The results are illustrated numerically for a particular choice of parameters

Keywords: Magnetic material, nano-tube, Green function.

PACS: 75.70. Ak

1. INTRODUCTION

In the last decade, there has been growing attention to the magnetic properties of materials at the nanoscales, such as nanowires, nanoparticles, nanofilms, nanobelts, nanotubes, nanorods etc [1-3]. The reason is that these materials have potential for applications in magneto-electronic devices. On the other hand, these systems show many new typical, peculiar, and unexpected magnetic properties that cannot be exhibit in bulk systems [4-6]. In the experimental area, the ferromagnetic nanotubes have been successfully synthesized by various methods and there magnetic properties have been investigated. Magnetic nanotubes have potential applications in ultrahigh-density magnetic storage devices, biotechnology, nanomedicine, information storage devices, and nanoelectronic devices etc [7-9].

In the theoretical area, the magnetic nanomaterials have been investigated within the various theoretical methods, such as effective- field theory (EFT) with correlations, Monte Carlo Simulations (MC_S), mean-field approximation (MFA), Green's function (GF) formalism [10-12].

Spin-wave excitations in ferromagnetic nanotube have recently been studied by a number of authors [5,6]. For example, A.L.Gonzalez, P.Landeros, Alvaro S.Nunes investigate the spin wave spectra associated to a vortex domain wall confined within a ferromagnetic nanotube [2]. Bin-Zhou Mi, Huai-Yu Wang Yun-Song Zhou developed a microscopic theory for magnetic behaviors of single-walled nanotubes use of the many-body Green's function method [6]. A nanotube can be modeled as having a chosen shape and size cross section (in the x-y

plane) with a finite number spins arranged. The magnetic properties of nanostructures are strongly dependent on the system shape and size.

2. MODEL AND FORMULATION

The schematic representation of nanotube with core-surface shell structure is displayed in fig.1. The black and white circles are magnetic atoms constituting the core and surface shell, respectively. The lines connecting them represent the nearest-neighbor exchange interaction. On the other hand, each spins is connected to the nearest-neighbor spins on the above and below section.

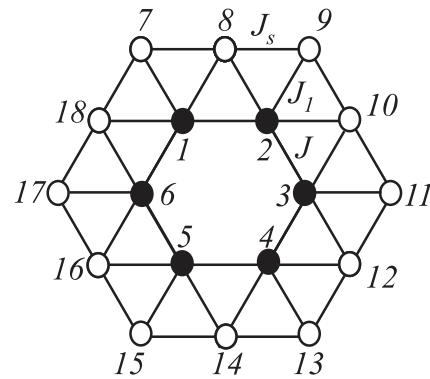


Fig.1. Schematic representation of a cylindrical nanotubes (side view). The nanotubes are infinite in the direction perpendicular to the axes z.

The system will be represented by the Hamiltonian

$$H = -J_s \sum_{i,\delta} S_i S_{i+\delta} - J \sum_{j,\delta} S_j S_{j+\delta} - J_l \sum_{l,m} S_l S_m - h \left(\sum_i S_i^z + \sum_j S_j^z \right) - D \left(\sum_i (S_i^z)^2 + \sum_j (S_j^z)^2 \right) \quad (1)$$

where J_s , J and J_l are the exchange coupling between two neighboring magnetic atoms at the shell surface, core and shell surface and core, respectively. S_i and S_j are spin operators, the sum δ is over nearest neighbors only

at surface and core. The second term of Eq. (1) describes the Zeeman interaction of the spins when an external magnetic field h applied along the z-direction, the last contribution is a single-ion anisotropy term (i.e. crystal field).

To study the magnetic properties of the nanotube under consideration, we evaluate a retarded GF of the form $\langle\langle S_i^+(t); S_j^-(t') \rangle\rangle$. After time Fourier transformation the retarded GF is denoted as $G_{i,j}(\omega) = \langle\langle S_i^+; S_j^- \rangle\rangle_\omega$,

$$\begin{cases} (\omega - h - D - 4J\langle S_c^z \rangle - 3J_1\langle S_s^z \rangle)G_{n,m}^{1,\tau} + J\langle S_c^z \rangle(G_{n,m}^{2,\tau} + G_{n,m}^{6,\tau} + G_{n+1,m}^{1,\tau} + G_{n-1,m}^{1,\tau}) + J_1\langle S_s^z \rangle(G_{n,m}^{18,\tau} + G_{n,m}^{8,\tau} + G_{n,m}^{7,\tau}) = \delta_{n,m}\delta_{1,\tau} \\ (\omega - h - D - 4J_s\langle S_s^z \rangle - J_1\langle S_c^z \rangle)G_{n,m}^{7,\tau} + J_s\langle S_s^z \rangle(G_{n,m}^{8,\tau} + G_{n,m}^{18,\tau} + G_{n+1,m}^{7,\tau} + G_{n-1,m}^{7,\tau}) + J_1\langle S_s^z \rangle G_{n,m}^{1,\tau} = \delta_{n,m}\delta_{7,\tau} \\ (\omega - h - D - 4J_s\langle S_s^z \rangle - 2J_1\langle S_c^z \rangle)G_{n,m}^{8,\tau} + J_s\langle S_s^z \rangle(G_{n,m}^{7,\tau} + G_{n,m}^{9,\tau} + G_{n+1,m}^{8,\tau} + G_{n-1,m}^{8,\tau}) + J_1\langle S_s^z \rangle(G_{n,m}^{1,\tau} + G_{n,m}^{2,\tau}) = \delta_{n,m}\delta_{8,\tau} \end{cases} \quad (2)$$

here n and m are layer indices, while $1, \dots, 18$ and τ label the position of the spins in layers n and m , respectively.

Now the GF is further Fourier transformed along the nanotube axis which periodic boundary condition. The total wave vector has two components $k_{tot} = (k, q)$. The system is periodic in the z direction, which lattice constant is a . According to Bloch's theorem has been employed for plane waves in order to receive the system equations [13,14]

$$G_{n\pm 1,m}^{(1,7,8),\tau} = \exp[\pm ika]G_{n,m}^{(1,7,8),\tau} \quad (3)$$

As for circumferential direction, the discrete Fourier transformed is taken with periodicity condition. One of wave vector component denoted as q takes the following values [6]:

$$q = \frac{\pi l}{3a} \quad l = 0, 1, 2, \dots, 5 \quad (4)$$

Then the Fourier transformation of the GF is written as

$$G_{n,m}^{(6,18),\tau} = \frac{1}{6} \sum_{l=0}^5 G_{n,m}^{(1,8),\tau} \exp[-iqa] ; G_{n,m}^{(2,9),\tau} = \frac{1}{6} \sum_{l=0}^5 G_{n,m}^{(1,7),\tau} \exp[iqa] \quad (5)$$

Using (3) and (5) the GF can be obtained by solving the equations (2)

$$G_{n,n}^{\tau,\tau} = \sum_{l=1}^3 \frac{\alpha_1(\omega_{kl})}{\omega - \omega_{kl}} + \sum_{l=4}^6 \frac{\alpha_4(\omega_{kl})}{\omega - \omega_{kl}} + \sum_{l=7}^9 \frac{\alpha_7(\omega_{kl})}{\omega - \omega_{kl}} + \sum_{l=10}^{11} \frac{\alpha_{10}(\omega_{kl})}{\omega - \omega_{kl}}; \quad \tau = (1, \dots, 6)$$

$$\alpha_1(\omega_{kl}) = \frac{(\omega_{k,l} - \lambda_s)^2 - J_1\langle S_c^z \rangle(\omega_{k,l} - \lambda_s) - J_s^2\langle S_s^z \rangle^2}{3 \prod_{j \neq l} (\omega_{kl} - \omega_{kj})}$$

$$\alpha_4(\omega_{kl}) = \frac{(\omega_{k,l} - \lambda_s)^2 - J_1\langle S_c^z \rangle(\omega_{k,l} - \lambda_s) - 3J_s^2\langle S_s^z \rangle^2}{3 \prod_{j \neq l} (\omega_{kl} - \omega_{kj})}$$

$$\alpha_7(\omega_{kl}) = \frac{(\omega_{k,l} - \lambda_s)^2 - J_1\langle S_c^z \rangle(\omega_{k,l} - \lambda_s) - 4J_s^2\langle S_s^z \rangle^2}{6 \prod_{j \neq l} (\omega_{kl} - \omega_{kj})}$$

$$\alpha_{10}(\omega_{kl}) = \frac{\omega_{k,l} - \lambda_s}{6(\omega_{k,l} - \omega_{k,j})} \quad (j \neq l) \quad (6a)$$

$$G_{n,n}^{\tau,\tau} = \sum_{l=1}^3 \frac{\beta_1(\omega_{kl})}{\omega - \omega_{kl}} + \sum_{l=4}^6 \frac{\beta_4(\omega_{kl})}{\omega - \omega_{kl}} + \sum_{l=7}^9 \frac{\beta_7(\omega_{kl})}{\omega - \omega_{kl}} + \sum_{l=10}^{11} \frac{\beta_{10}(\omega_{kl})}{\omega - \omega_{kl}}, \quad \tau = (7, 9, 11, \dots, 17)$$

$$\beta_1(\omega_{kl}) = \frac{(\omega_{k,l} - \lambda_c)(\omega_{k,l} - \lambda_s) - J_1 \langle S_c^z \rangle (\omega_{k,l} - \lambda_c + J_1 \langle S_s^z \rangle) - J \langle S_c^z \rangle (\omega_{k,l} - \lambda_s - J_1 \langle S_c^z \rangle)}{3 \prod_{j \neq l} (\omega_{kl} - \omega_{kj})}$$

$$\beta_4(\omega_{kl}) = \frac{(\omega_{k,l} - \lambda_c)(\omega_{k,l} - \lambda_s) - J_1 \langle S_c^z \rangle (\omega_{k,l} - \lambda_c + 3J_1 \langle S_s^z \rangle) + J \langle S_c^z \rangle (\omega_{k,l} - \lambda_s - J_1 \langle S_c^z \rangle)}{3 \prod_{j \neq l} (\omega_{kl} - \omega_{kj})} \quad (6b)$$

$$\beta_7(\omega_{kl}) = \frac{(\omega_{k,l} - \lambda_c)(\omega_{k,l} - \lambda_s) - J_1 \langle S_c^z \rangle (\omega_{k,l} - \lambda_c + 4J_1 \langle S_s^z \rangle) + 2J \langle S_c^z \rangle (\omega_{k,l} - \lambda_s - J_1 \langle S_c^z \rangle)}{6 \prod_{j \neq l} (\omega_{kl} - \omega_{kj})}$$

$$\beta_{10}(\omega_{kl}) = \frac{\omega_{k,l} - \lambda_c - 2J \langle S_s^z \rangle}{6(\omega_{k,l} - \omega_{k,j})}$$

$$G_{n,n}^{\tau,\tau} = \sum_{l=1}^3 \frac{\gamma_1(\omega_{kl})}{\omega - \omega_{kl}} + \sum_{l=4}^6 \frac{\gamma_4(\omega_{kl})}{\omega - \omega_{kl}} + \sum_{l=7}^9 \frac{\gamma_7(\omega_{kl})}{\omega - \omega_{kl}} + \frac{1}{6(\omega - \omega_{k12})}; \quad \tau = (8, 10, 12, \dots, 18)$$

$$\gamma_1(\omega_{kl}) = \frac{J_1^2 \langle S_c^z \rangle \langle S_s^z \rangle - (\omega_{k,l} - \lambda_s)(\omega_{k,l} - \lambda_c - J \langle S_c^z \rangle)}{3 \prod_{j \neq l} (\omega_{kl} - \omega_{kj})}$$

$$\gamma_4(\omega_{kl}) = \frac{-J_1^2 \langle S_c^z \rangle \langle S_s^z \rangle + (\omega_{k,l} - \lambda_s)(\omega_{k,l} - \lambda_c + J \langle S_c^z \rangle)}{3 \prod_{j \neq l} (\omega_{kl} - \omega_{kj})} \quad (6c)$$

$$\gamma_7(\omega_{kl}) = \frac{-J_1^2 \langle S_c^z \rangle \langle S_s^z \rangle + (\omega_{k,l} - \lambda_s)(\omega_{k,l} - \lambda_c + 2J \langle S_c^z \rangle)}{6 \prod_{j \neq l} (\omega_{kl} - \omega_{kj})}$$

$$\lambda_c = h + D + 3J_1 \langle S_s^z \rangle + 2J \langle S_c^z \rangle (2 - \cos ka), \quad \lambda_s = h + D + J_1 \langle S_c^z \rangle + 2J_s \langle S_s^z \rangle (2 - \cos ka)$$

The poles of the Green functions occur at energies, which are the roots of the spin wave dispersion equation for the nanotubes under consideration:

$$\omega_{ki} = -2r_i \cos(\varphi_i/3) + b_i/3, \quad i = 1, 4, 7$$

$$\omega_{ki} = 2r_{i-1} \cos((\pi - \varphi_{i-1})/3) + b_{i-1}/3, \quad i = 2, 5, 8$$

$$\omega_{ki} = 2r_{i-2} \cos((\pi + \varphi_{i-2})/3) + b_{i-2}/3, \quad i = 3, 6, 9$$

(7)

$$\omega_{k10} = 0.5(2J\langle S_c^z \rangle + \lambda_c + \lambda_s) + 0.5\sqrt{(2J\langle S_c^z \rangle + \lambda_c + \lambda_s)^2 + 4(J_1^2\langle S_c^z \rangle\langle S_s^z \rangle - 2J\lambda_c\langle S_c^z \rangle - \lambda_c\lambda_s)}$$

$$\omega_{k11} = 0.5(2J\langle S_c^z \rangle + \lambda_c + \lambda_s) - 0.5\sqrt{(2J\langle S_c^z \rangle + \lambda_c + \lambda_s)^2 + 4(J_1^2\langle S_c^z \rangle\langle S_s^z \rangle - 2J\lambda_c\langle S_c^z \rangle - \lambda_c\lambda_s)}$$

$$\omega_{k12} = J_1\langle S_c^z \rangle + \lambda_s$$

where

$$r_i = \sqrt{|3c_i - b_i^2|}/3, \quad \varphi_i = \arccos\left(\frac{2b_i^3 - 9b_i c_i + 27d_i}{2\sqrt{(3c_i - b_i^2)^3}}\right) \quad i = 1, 4, 7$$

$$b_1 = -(J + J_1)\langle S_c^z \rangle - \lambda_c - 2\lambda_s$$

$$c_1 = -2J_1^2\langle S_c^z \rangle\langle S_s^z \rangle - J_s^2\langle S_s^z \rangle^2 + J_1\langle S_c^z \rangle(J\langle S_c^z \rangle + \lambda_c + \lambda_s) + \lambda_s(2J\langle S_c^z \rangle + 2\lambda_c + \lambda_s)$$

$$d_1 = J_1^3\langle S_c^z \rangle^2\langle S_s^z \rangle + (J\langle S_c^z \rangle + \lambda_c)(J_s^2\langle S_s^z \rangle^2 - \lambda_s^2 - J_1\langle S_c^z \rangle\lambda_s) + 2J_1^2\langle S_c^z \rangle\langle S_s^z \rangle(J_s\langle S_s^z \rangle + \lambda_s)$$

$$b_4 = (J - J_1)\langle S_c^z \rangle - \lambda_c - 2\lambda_s$$

$$c_4 = -4J_1^2\langle S_c^z \rangle\langle S_s^z \rangle - 3J_s^2\langle S_s^z \rangle^2 + J_1\langle S_c^z \rangle(-J\langle S_c^z \rangle + \lambda_c + \lambda_s) + \lambda_s(-2J\langle S_c^z \rangle + 2\lambda_c + \lambda_s)$$

$$d_4 = J_1^3\langle S_c^z \rangle^2\langle S_s^z \rangle - (J\langle S_c^z \rangle - \lambda_c)(3J_s^2\langle S_s^z \rangle^2 - \lambda_s^2 - J_1\langle S_c^z \rangle\lambda_s) + 2J_1^2\langle S_c^z \rangle\langle S_s^z \rangle(3J_s\langle S_s^z \rangle + 2\lambda_s)$$

$$b_7 = (2J - J_1)\langle S_c^z \rangle - \lambda_c - 2\lambda_s$$

$$c_7 = -5J_1^2\langle S_c^z \rangle\langle S_s^z \rangle - 4J_s^2\langle S_s^z \rangle^2 + J_1\langle S_c^z \rangle(-2J\langle S_c^z \rangle + \lambda_c + \lambda_s) + \lambda_s(-4J\langle S_c^z \rangle + 2\lambda_c + \lambda_s)$$

$$d_7 = J_1^3\langle S_c^z \rangle^2\langle S_s^z \rangle - (2J\langle S_c^z \rangle - \lambda_c)(4J_s^2\langle S_s^z \rangle^2 - \lambda_s^2 - J_1\langle S_c^z \rangle\lambda_s) + J_1^2\langle S_c^z \rangle\langle S_s^z \rangle(8J_s\langle S_s^z \rangle + 5\lambda_s)$$

Solving the average spin, we derive the correlation function $\langle S^- S^+ \rangle$ using the spectrum theorem [14,15]

$$\langle S^- S^+ \rangle = -\frac{2S}{N\pi} \sum_k \int_{-\infty}^{\infty} d\omega \frac{\text{Im}G(k, \omega + i\varepsilon)}{e^{\beta\omega} - 1} \quad (8)$$

Here $\beta = 1/k_B T$, k_B is the Boltzmann constant, T is the temperature. Using (5) and the relation $1/(x + i\varepsilon) = \text{P}(1/x) - i\pi\delta(x)$ to obtain the imaginary part of the Green functions, one finally obtains

$$\begin{aligned}\langle S_{n,\tau}^- S_{n,\tau}^+ \rangle &= -\frac{2S}{N} \sum_k \left(\sum_{l=1}^3 \frac{\alpha_l(\omega_{kl})}{e^{\beta\omega_{kl}} - 1} + \sum_{l=4}^6 \frac{\alpha_l(\omega_{kl})}{e^{\beta\omega_{kl}} - 1} + \sum_{l=7}^9 \frac{\alpha_l(\omega_{kl})}{e^{\beta\omega_{kl}} - 1} + \sum_{l=10}^{11} \frac{\alpha_l(\omega_{kl})}{e^{\beta\omega_{kl}} - 1} \right) \quad \tau = 1, 2, \dots, 6 \\ \langle S_{n,\tau}^- S_{n,\tau}^+ \rangle &= -\frac{2S}{N} \sum_k \left(\sum_{l=1}^3 \frac{\beta_l(\omega_{kl})}{e^{\beta\omega_{kl}} - 1} + \sum_{l=4}^6 \frac{\beta_l(\omega_{kl})}{e^{\beta\omega_{kl}} - 1} + \sum_{l=7}^9 \frac{\beta_l(\omega_{kl})}{e^{\beta\omega_{kl}} - 1} + \sum_{l=10}^{11} \frac{\beta_l(\omega_{kl})}{e^{\beta\omega_{kl}} - 1} \right) \quad \tau = 7, 9, \dots, 17 \\ \langle S_{n,\tau}^- S_{n,\tau}^+ \rangle &= -\frac{2S}{N} \sum_k \left(\sum_{l=1}^3 \frac{\gamma_l(\omega_{kl})}{e^{\beta\omega_{kl}} - 1} + \sum_{l=4}^6 \frac{\gamma_l(\omega_{kl})}{e^{\beta\omega_{kl}} - 1} + \sum_{l=7}^9 \frac{\gamma_l(\omega_{kl})}{e^{\beta\omega_{kl}} - 1} + \frac{1}{6(e^{\beta\omega_{k12}} - 1)} \right) \quad \tau = 8, 10, \dots, 18\end{aligned}\quad (9)$$

According to the theory of Callen [16] the average spin can be calculated using the following equation

$$\langle S^z \rangle = \frac{(S+1+\Phi)\Phi^{2S+1} + (S-\Phi)(1+\Phi)^{2S+1}}{\Phi^{2S+1} - (1+\Phi)^{2S+1}} \quad (10)$$

where $\Phi = \frac{\langle S^- S^+ \rangle}{2\langle S^z \rangle}$

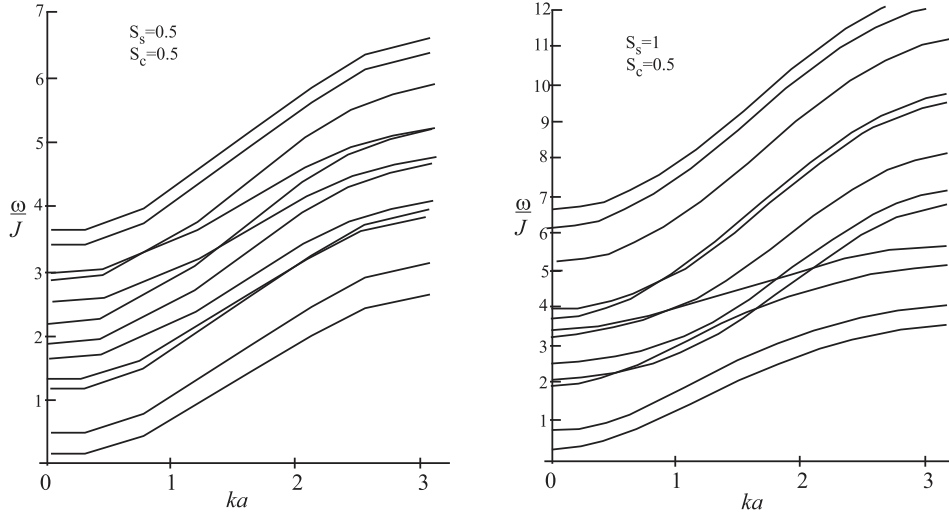


Fig. 2. Spin wave frequency versus wave number ka for the nanotubes under consideration with parameters $h/J = 0.2$, $D/J = 0.1$, $J_1/J = 0.5$, $J_s/J = 1.5$.

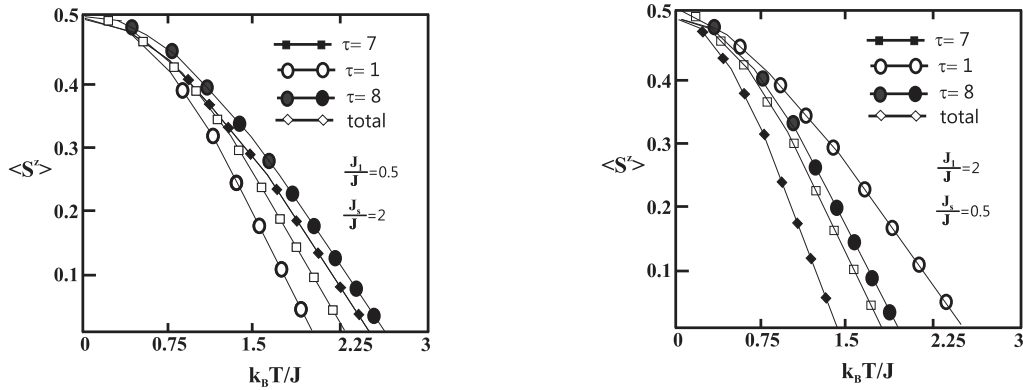


Fig. 3. Temperature dependence of the spin magnetization for the parameters $h/J = 0.2$, $D/J = 0.1$, $S_c = S_s = 0.5$

Now the equation (8) and (9) can be solved self consistently to obtain the average spin at any given temperature.

If $S = 1/2$ $\langle S^z \rangle = \frac{1}{2} - \langle S^- S^+ \rangle$.

3. CONCLUSIONS

In this paper, we present the theory of spin-wave excitations of a cylindrical ferromagnetic nanotubes. Dispersion equations of spin waves propagating along the nanotubes, and temperature dependence of magnetizations for nanotube with core/shell structure have been studied. Fig. 2 shows spin-wave spectra for reduced frequency ω/J versus ka for nanotubes under consideration. The frequencies for the lowest branches are not zero at $ka = 0$. Easily, it can be explained by applied external magnetic field and single-ion anisotropy. The spin wave frequencies increase with increasing wave vectors and exchange coupling between spins. On the other hand, with increasing value of the spins spin wave frequencies increase. It can be verified from these results that when $J_1 = 0$ for the nanotubes depicted in fig.1 they reduces for the two magnetic single-walled nanotubes.

The temperature dependence of magnetization in the nanotubes under consideration is demonstrated in fig. 3. The spontaneous magnetization of the spins at zero

temperature is $\langle S^z \rangle = 0.5$. The magnetizations decrease continuously with increasing values of temperature, and they become zero at critical temperature; therefore a second-order phase transition occurs. We illustrate the magnetization versus reduced temperature for $J_1/J = 0.5$, $J_s/J = 2$ and $J_1/J = 2$, $J_s/J = 0.5$, respectively. In the each case, the total spin magnetization has the middle value. If exchange interaction between magnetic atoms at surface grows weaker, then their magnetizations are weaker than that of core spins. Magnetization of the surface spins labeled $\tau = 7, 9, 11, 13, 15, 17$ is smaller than that of the spins labeled $\tau = 8, 10, 12, 14, 16, 18$. This will be able to understand clearly. For example, surface spin labeled $\tau = 7$ exchange interacts with one core spin labeled $\tau = 7$, while spin labeled $\tau = 8$ with two core spins $\tau = 1$ and $\tau = 2$. But in particular case, when $J_1 = 0$ all spins has the same orientation and the curves coincide.

-
- [1] T.M. Nguyen and M.G. Cottam. Surface Science 600, 4151-4154 (2006)
 - [2] A.L. Gonzalez, P. Landeros, Alvaro S. Nunes. Journal of Magnetism and Magnetic Materials 322, p.530-535, (2010).
 - [3] T. Kaneyoshi. Phys.Status Solidi B 248 No 1 250-258 (2011)
 - [4] Ersin Kantar, Yusuf Kocakaplan. Solid State Communications 177, 1-6 (2014)
 - [5] C.D.Salazar-Enriques,E.Restrepo-Parra. J. Restrepo Physica E 52 (2013) 86-91.
 - [6] Bin-Zhou Mi, Huai-Yu Wang, Yun-Song Zhou. Journal of Magnetism and Magnetic Materials 322, p.952-958, (2010).
 - [7] O. A. Tretiakov and Ar. Abanov. Phys. Rev. Lett. 105, 157201 (2010)
 - [8] V.S. Tkachenko, V.V. Kruglyak, A.N. Kuchko. Phys.Rev. B 81, 024425 (2010)
 - [9] Z. K. Wang, M. H. Kuok, S. C. Ng, D. J. Lockwood, M. G. Cottam, K. Nielsch, R. B. Wehrspohn, and U. Gösele. Phys. Rev. Lett. v.89, n.2, 027201 (2002)
 - [10] V.A. Tanriverdiyev. Journal of Magnetism and Magnetic Materials 393, (2015) 188-191
 - [11] V.V. Kruglyak, R.J. Hicken, A.N.Kuchko, V.Yu. Gorobets. Journal of Applied Physics 98, (2005) 014304.
 - [12] T.M. Nguyen and M.G. Cottam. Phys.Rev. B 71, (2005) 094406.
 - [13] V.A. Tanriverdiyev, V.S. Tagiyev, S.M. Seyid-Rzayeva. FNT 12 (2003).
 - [14] H.T. Diep. Phys.Lett. A 138, 69 (1989)
 - [15] R. Schiller and W. Nolting. Phys. Rev. B 60, 462-471 (1999)
 - [16] Callen H B. Phys. Rev. 130 890 (1963)

Receivied: 06.02.2017

SUPERIONIC CONDUCTION IN TlGaSe_2 CRYSTAL INDUCED BY γ -IRRADIATION

R.M. SARDARLI, N.A. ALIYEVA, F.T. SALMANOV, A.P. ABDULLAYEV,
M.Y. YUSIFOV, A.A. ORUDJEVA

*Institute of Irradiation Problems of Azerbaijan National Academy of Sciences,
B.Vakhabzade 9, AZ1143*

The component frequency dependences of total complex impedance are measured in $25 \div 10^6$ Hz spectral region by impedance spectroscopy method and relaxation processes in TlGaSe_2 crystal before and after irradiation exposure by dose in 25 Mrad are investigated. The decrease of relaxation time in crystal after irradiation exposure is revealed. The obtained diagrams on complex plane ($Z''-Z'$) are analyzed using the method of equivalent replacement circuits. It is shown that the phase transition takes place with system transition into superionic state after γ – irradiation.

Keywords: impedance spectroscopy, γ – irradiation, equivalent circuit

PACS: 71.23.An

1. INTRODUCTION

Thallium chalcogenides of third group of Periodic table are characterized by laminar and laminar-chain structure and compounds based on these materials are widely researched [1-10] and also they are widely used in practices. The single crystals of these compounds are characterized by high sensitivity in IR, visible and roentgen region of electromagnetic wave spectrum and have the high tensosensitivity. Because of these properties, the compounds related to this group ($\text{TlB}^{\text{III}}\text{C}^{\text{VI}}_2$) are used and can be used as functional elements in optoelectronic systems as photoresistors, photodetectors, roentgenodetectors and nuclear radiation detectors and etc [11,12].

The electric conduction and dielectric properties of TlGaTe_2 , TlInSe_2 and TlInTe_2 compounds at temperatures higher 300K are studied in works [2-4, 13-15]. The superionic conduction the mechanism of which is connected with Tl^+ ion diffusion is revealed. These compounds reveal the effect of negative differential resistance and voltage oscillation (the nature of which isn't established).

The decrease of electric conduction in electrostatic field is revealed at TlInSe_2 crystal investigation in constant and alternative electric field in temperature region 100-400K [18]. The complex impedance spectra are measured in $25 \div 10^6$ Hz frequency range, analysis of diagrams in complex plane ($Z''-Z'$) with use of method of equivalent circuits is carried out. These investigations show that electric properties of TlInSe_2 crystals are defined by hopping conduction in investigated interval of frequencies and temperatures and charge accumulation on limiting contacts takes place in this case. These investigations show that TlGaTe_2 , TlInSe_2 and TlInTe_2 compounds have the enough high mobility of thallium ions and can be considered as materials with mixed electronic-ion conduction. Such conduction character shows on usage availability of these materials in the capacity of ionistors and accumulators.

The investigations of impedance characteristics of TlGaTe_2 , TlInSe_2 and TlInTe_2 compounds in frequency region $25 \div 10^6$ Hz show that relaxation processes connected with charge transfer accelerate at increase of

disorder degree. The crystal transition effect into superionic state induced by field is revealed in TlGaTe_2 crystal [15].

The analysis of earlier carried investigations shows that further investigations of thallium chalcogenide compounds joint by general formula $\text{TlB}^{\text{III}}\text{C}^{\text{VI}}_2$ presents is of big interest. The investigations of kinetic characteristics in TlGaSe_2 crystal are carried out with the aim of expansion of earlier carried investigations, understanding of superionic state nature and relaxation processes taking place there. The investigations are carried out before and after irradiation exposure by γ -quantums with energy ≈ 1 MeV (1.17 and 1.33 MeV) on ^{60}Co at room temperature with use of impedance spectroscopy method.

2. EXPERIMENT

The solid solution samples are synthesized by alloying of initial components (purity not less 99.99) in evacuated quartz ampoules and their single crystals are grown up by Bridgeman modified method. The freshly cleaved samples in which "c" crystal axis is perpendicularly oriented to cleavage, prepared for investigation, have the rectangular form.

The condensers in which the plates of the investigated materials serve as dielectrics are prepared for measurements of temperature dependences of TlGaSe_2 crystal electric conduction. The capacitor plates are obtained by coating of argentum conducting contacts on the surface of cleaved plates. The sample electric properties are investigated by impedance spectroscopy method in frequency region $25 \div 10^6$ Hz. The electric conduction investigations are carried out by immittance measurer E7-25, the measurement precision is 0,1%. The samples are exposed by influence of γ -irradiation from standard irradiation source ^{60}Co after preliminary measurements. The irradiation dose is gradually accumulated by the means of the consistent expositions of γ -influence up to value 25 Mrad.

3. EXPERIMENTAL RESULTS AND THEIR DISCUSSION

As it is known, the impedance measurement data can be presented in the form of the hodograph impedance on

complex plane. The obtained data are presented in the form of circular arcs which can be regular or irregular shapes. At the same time the equivalent replacement circuit from joint capacities and resistances describing the corresponding arc form. In such construction the current

frequency in graphics isn't shown as a rule. The presence of the frequency dependences of impedance components in Bode diagram form allows us to detail analyze the spectral characteristics of real and imaginary impedance component.

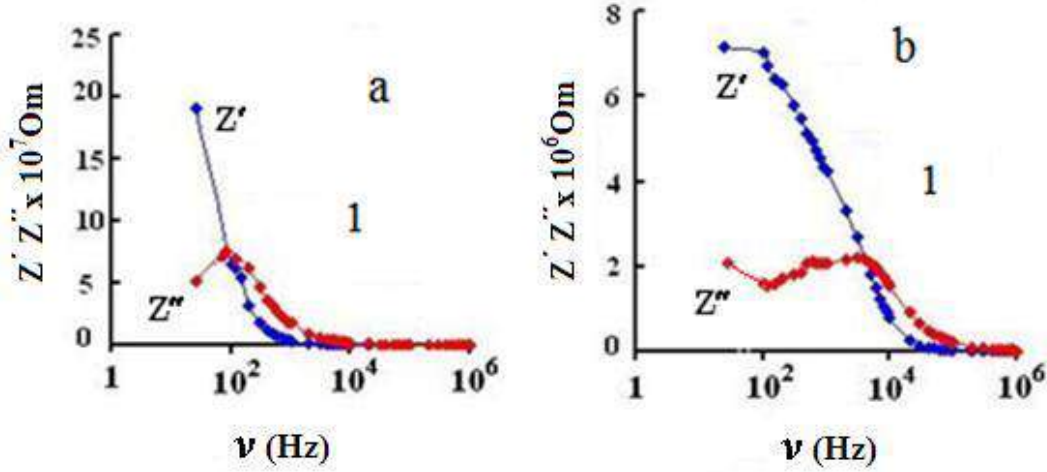


Fig.1. The frequency dependences of real (Z') and imaginary (Z'') of impedance component for TiGaSe₂ sample. *a* figure are the measurements carried out before γ - irradiation and *b* figure are the measurements after γ - irradiation.

The frequency dependences of real (Z') and imaginary (Z'') parts of impedance of TiGaSe₂ crystal are given in semilogarithmic scale in fig.1(a,b).

The presented dependences have the form corresponding to parallel equivalent replacement circuit. The measurements are carried out before and after γ – irradiation.

The frequency values (f_{\max}), corresponding to Z'' maximum, (τ) relaxation times, frequencies (f_{jump}) corresponding to beginning of TiGaSe₂ frequency dispersion before and after γ -irradiation are shown in tables. The measurements are carried at room temperature.

Mrad	f_{\max} , kHz	$\tau=1/2\pi f_{\max}$	f_{jump} , kHz
0	0.1	$1,6 \cdot 10^{-3}$	1
25	5	$3,18 \cdot 10^{-5}$	5
			0

As it is seen from the figures, Z'' maximum value coincides with Z' value at definite frequencies. This fact confirms that the hodograph arc (fig.2) describes the curve close to semicircle with maximum in intersection points of Z' and Z'' and center situated on real axis. Such dependence type corresponds to parallel equivalent replacement circuit (fig.3a). Moreover, the charge transfer is characterized by same relaxation time.

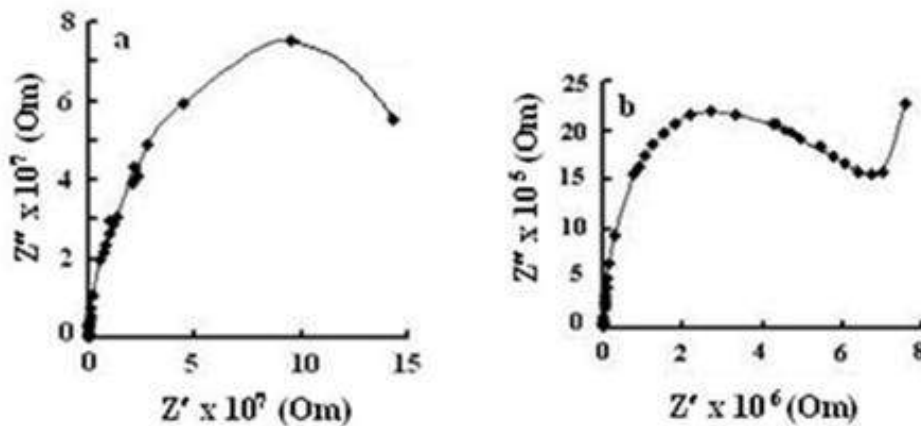


Fig.2. The diagram on complex plane (Z'' - Z') obtained on the base of fig.1. The figure *a* are the measurements carried out before γ - irradiation, figure *b* are the measurements after γ -irradiation.

The diagram on complex plane (Z'' - Z') obtained on base of data fig.1 are presented in fig.2. The frequency values (f_{\max}) corresponding to ($-\text{Im}Z$) maximum, relaxation times (τ), frequencies corresponding to frequency dispersion beginning (f_{jump}) for TlGaSe_2 samples before and after γ -irradiation, are given in table. As it is seen from the table, f_{\max} frequency increase corresponding to Z'' maximum is observed. This means that charge transfer is accompanied by decrease of relaxation time (table). The spectrum analysis allows us to conclude that the relaxation process acceleration after irradiation influence is observed in TlGaSe_2 crystal samples.

As it is seen from fig. 1, the impedance imaginary parts reveal the maximum at f_{\max} frequencies corresponding to condition $C_{\text{eff}}R_{\text{eff}}\omega_{\max} = 1$, where C_{eff} and R_{eff} are effective parameters of equivalent circuit, $\omega_{\max} = 2\pi f_{\max}$ is circular frequency. The corresponding impedance hodographs of TlGaSe_2 crystal and the measurements are carried out at 300K before and after irradiation exposure by 25Mrad dose are given in fig.2. The top of hodograph arc corresponds to ω_{\max} resonance frequency.

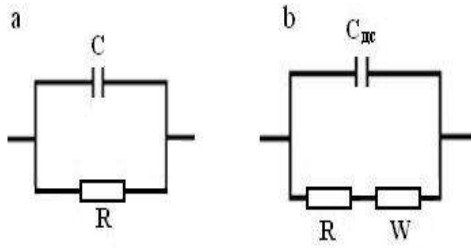


Fig.3. Equivalent circuit (**a** is before γ - irradiation, **b** is after it) for electrode with capacity of C_{DL} double layer, W is Warburg diffuse impedance, R is sample resistance.

It is seen that arc has the form close to semicircle the center of which locates on real axis at measurements carried out before γ - irradiation; moreover, the charge transfer is characterized by same relaxation time. In this case the impedance hodograph of TlGaSe_2 crystal is qualitatively and quantitatively described in approximation of equivalent circuits with the help of impedance components of model electric circuit. Such hodograph form corresponds to homogeneous sample with low-ohmic and non-blocking contacts. The equivalent circuit of such hodograph is given in fig. 3a. The elements of equivalent circuit R and C can directly correspond to resistance and capacity of measurable sample.

The diagrams on complex plane (Z'' - Z') obtained from measurements after influence of γ -quanta, present themselves semicircles for one parallel RC-chain and beams in diagram low-frequency region (fig.2, curve **b**). These beams on impedance diagram are probably connected with Warburg diffuse impedance on the basis of which the carrier diffusion doesn't achieve the near-contact layer boundary in frequency range of applied sinusoidal signal. The crystal transition in superionic state is caused with system disorder in the

result of irradiation influence can be responsible for appearance of Warburg diffuse impedance.

Earlier it has been shown in [2-4, 13-15] that the peculiarities connected with existence of ion conduction reveal at temperatures higher 300K in $\text{A}^{\text{III}}\text{B}^{\text{III}}\text{C}^{\text{VI}}_2$ crystal group. In this case Tl^{+1} ions diffusing in crystal can be responsible for existence of Warburg diffuse impedance in hodographs of investigated crystals after system transition in superionic state, moreover, the defects caused by irradiation influence are factor promoting ion mobility.

The observable difference in obtained hodographs and corresponding equivalent circuits can explain within framework of interaction theory between gamma quanta with substance.

As it is known [16], the irradiation influence on solid state leads to formation of non-equilibrium defects; this can be Frenkel couples, vacancies, interstitial atoms and etc. The weakening of beam intensity takes place at passing of γ -irradiation (in our case gamma quantum energy is $\sim 1\text{MeV}$) through the substance. The electrons which lead to defect formation in crystal lattice generate. The contribution in total scattering cross-section in this gamma-quantum energy region is the incoherent scattering on substance electrons (Kompton effect). The effective cross-section of Kompton scattering calculated per one atom proportionally to atomic number $\sigma'_c = Z \cdot \sigma_c$. As Tl is the largest atom in TlGaSe_2 crystal, then thallium atoms will be probable element which will shift. Note that the photonuclear reaction threshold isn't achieved at gamma-quantum energy in $\sim 1\text{MeV}$.

4. IONIC CONDUCTION

The temperature dependence of electric conduction ($\sigma(T)$) for TlGaSe_2 crystal is given in fig.4). The measurements are carried out at electric field direction along crystal monoclinic axis, (**a**) is curve that represents the measurements carried out before the gamma irradiation, (**b**) is curve that represents the measurements carried out after gamma irradiation. As it is seen from the figure (**a** curve) the insignificant conduction increase at 450K is observed on crystals which aren't exposed to gamma irradiation, however, the jump in $\sigma(T)$ dependence and further conduction increase with activation energy 0.04eV at gamma influence 25 Mrad. As it is seen from figure insert the experimental points (in both before and after irradiation) of temperature dependence $\ln\sigma(T)$ in region of electric conduction strong jump well locate on direct line which is described by equation [17-19] for the case of ionic conduction:

$$\sigma T = \sigma_0 \cdot \exp(-\Delta E/kT) \quad (1)$$

here ΔE is electric conduction activation energy, k is Boltzmann constant.

The observable hopping change of electric conduction in TlGaSe_2 crystal exposed by gamma irradiation can be explained by strong change of ion number in states where they have the high mobility, i.e. phase transition in superionic state.

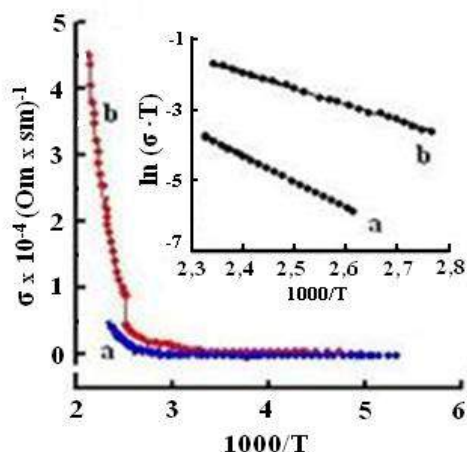


Fig.4. Temperature dependence of TiGaSe_2 crystal conduction in Arrhenius coordinates. $\ln(\sigma \cdot T)$ dependence on $1000/T$ is given in insert. **a** curve represents the measurement results carried out before gamma irradiation, **b** curve represents the measurements after it.

TiGaSe_2 crystalline structure consists in anionic layers formed by $\text{Ga}_4\text{Se}_{10}$ tetrahedrals which consist in four GaSe_4 tetrahedrals [9]. Ti^+ ions locate in trigonal voids. It is supposed from chemical analysis of crystal that the layered structure of TiGaSe_2 crystal and Ti^+ ion

position in trigonal voids mostly cause to thallium ion mobility.

The linear character of $\ln(\sigma \cdot T)$ on $1/T$ is higher than temperature jump (insert to figure 1) shows the dominant character of ion conduction higher critical temperature. The presence of layers with weak Van-der-Waals interaction and also Ti^+ ion position in trigonal voids allows us to conclude that phase transition in superionic state caused by thallium ion diffusion by vacancies in thallium sublattice takes place. The gamma irradiation causes to disorder (melting) in thallium sublattice in TiGaSe_2 crystal. Such conduction is typical for materials with dominant ion conduction type [2,17-19].

4. CONCLUSION

The characteristic times of relaxation processes in TiGaSe_2 crystal before and after γ -irradiation are measured by impedance spectroscopy methods. The decrease of relaxation time in TiGaSe_2 after gamma irradiation is revealed. The energy loss mechanism in crystal in alternative field consists in both losses connected with through conduction and losses connected with relaxation polarization. The phase transition in superionic state at temperature 450K after γ -irradiation connected with disorder of thallium sublattice caused by irradiation influence, is revealed.

- [1] N. Mamedov, K. Wakita, S. Akita, Y. Nakayama. "1D- TiInSe_2 : BandStructure, Dielectric Function and Nanorods", "Japanese Journal of Applied Physics" vol. 44, No.1B, 2005, pp. 1-6.
- [2] R.M. Sardarly, O.A. Samedov, A.P. Abdullaev, F.T. Salmanov, A. Urbanovic, F. Garet. J-L. Japanese Journal of Applied Physics, 50 (2011) 05FC09 1-2.
- [3] P.M. Sardarly, O.A. Samedov, A. Sardarli, N.A. Aliyeva, R.Sh. Aqayeva, T. Musazade. "Superionic Conduction and Specific Effects Induced by γ - Irradiation in Nanofibrous TiGaTe_2 Crystals", "International Journal of Theoretical and Applied Nanotechnology", Vol.1, Issue 1, 2012, pp.20-28.
- [4] P.M. Sardarly, O.A. Samedov, A.P. Abdullaev, F.T. Salmanov. FTT, 2011, t.53, v.8, str. 1488-1492. (In Russian).
- [5] A.U. Sheleg, E.M. Zub, A.Ya. Yachkovskii, S.N. Mustafaeva and E.M. Kerimova. "X-ray diffraction study of $(\text{TiInSe}_2)_{1-x}(\text{TiGaTe}_2)_x$ crystal system" Crystallography Reports", 2012, vol.57, no.2, pp.283-285.
- [6] S.N. Mustafaeva, E.M. Kerimova, S.S. Abdinbekov, L.N. Alieva, A.I. Hasanov, S.G. Jafarova. "Electro physic sof $(\text{TiInSe}_2)_{0.1}(\text{TiGaTe}_2)_{0.9}$ " ICTRE-2012, N.68, pp.332-334.
- [7] K.R. Allakhverdiev, E.A. Vinogradov, N.M. Melnik, M.A. Nizametdinova, E.Yu. Salaev, R.M. Sardarly. "Vibration Properties of TiSe " Phys.Stat.Sol.(b) 1978, v.87, pp.K115-K117.
- [8] R.M. Gasanly, A.F. Goncharov, B.M. Dzhavadov, N.M. Melnik, V.I. Tagirov, E.A. Vinogradov. "Vibrational spectra of TiGaTe_2 , TiInTe_2 and TiInSe_2 layer crystals" Phys. Stat. Sol.(b) 1980, v.97, pp.367-377.
- [9] A.M. Panich, R.M. Sardarly. "Physical Properties of the Low Dimensional A^3B^6 and $\text{A}^3\text{B}^3\text{C}^6_2$ Compounds" <Nova Science Publishers> NY, 2010, p.310.
- [10] M.V. Belausov, P.M. Sardarly. FTT, 1985, t.27, v.3 s.662-668. (In Russian).
- [11] E.Yu. Salaev, K.P. Allaxverdiev, Sh.G. Gas;mov, T.G. Mamedov. Datchik gidrostaticheskogo davleniya. Avtorskoe svideetelstvo SSSR № 1182291, 1984. (In Russian).
- [12] I.V. Alekseev, S.V. Rozov. Dedektor yadernogo izlucheniya. Patent № 80070, 2009. (In Russian).
- [13] R.M. Sardarly, O.A. Samedov, A.P. Abdullaev, E.K. Guseynov, F.T. Salmanov, G.R. Safarova. FTT, 44, 610 (2010). (In Russian).
- [14] R.M. Sardarly, O.A. Samedov, A.P. Abdullaev, F.T. Salmanov, O.Z. Alekperov, E.K. Guseynov, N.A. Alieva. FTT, 45,1441 (2011). (In Russian).
- [15] R.M. Sardarly, O.A. Samedov, A.P. Abdullaev, E.K. Guseynov, E.M. Godjaev, F.T. Salmanov. FTT, 45, 1009 (2011). (In Russian).
- [16] V.V. Galavanov. FTT, 1959, t.1, vip.3, s.432-441. (In Russian).
- [17] A.S. Nowick, A.V. Vaysleyb, I. Kuskovsky. Phys. Rev. B **58**,8398 (1998).
- [18] Yu.Ya. Gurevich, Yu.I. Xarkach. UFN, 136, 693 (1982). (In Russian).
- [19] Yu.I. Xarkach. FTT, 23, 2190 (1981). (In Russian).

Recevid:08.02.2017

CURRENT OSCILLATIONS IN SEMICONDUCTORS WITH DEEP TRAPS IN STRONG ELECTRIC AND MAGNETIC FIELDS

E.R. GASANOV, A.V. ISLAMZADE, R.A. GASANOVA

BSU, Institute of Physical Problems¹

AZ -1148, Baku, Z.str, 23

Institute of Physics of Azerbaijan National Academy of Sciences

AZ -1143, Baku, G.Javid ave., 131

aygul_islamzade@mail.ru

The external instability theory in definite impurity semiconductors at $E_0 \sim H^4$ is constructed. It is shown that longitudinal current oscillations at $E_0 \sim H_0$ take place in two extreme cases 1) current oscillation frequency is bigger than all character frequencies; 2) current frequency oscillations is less than all character frequencies.

The values of electric fields and current oscillation frequency are found in both cases. In all calculations is accepted that R active resistance and positive reactive resistance have the values $R = R_1 = Z_0$. The dependences $E_0(H)$, $\omega(H)$ in all limited cases are constructed.

Keywords: instability, oscillations, frequency, electric field, ohmic resistance, reactance.

PACS: 72.20.Jv, 78.20.Jy, 78.40.Fy, 73.50

The many works [1-5] are dedicated to experimental and theoretical investigations of current instability in semiconductors and appearing oscillating phenomena in them. The appearance of such quantity of works is connected with possibility of practical use of current instability phenomena in semiconductors for formation of high-frequency generators, amplifiers and also the tendency to develop the theory models for explanation of various reasons of instability appearance in semiconductors. The negative differential conductivity appears in strong electric field in the result of the dependence of current carrier trapping in semiconductor. The presence of negative conduction leads to appearance of current oscillations. The capture rate of charge carriers by impurity center in semiconductor strongly depends on charge carrier energy. The electric field presence increases the charge carrier energy; moreover, charge carrier capture rate depends on electric field. Consequently, the steady-state concentration of charge carriers in conduction band changes. At constant value of lattice temperature the recombination rate and generation rate changes only by electric field. The electron capture (recombination) increases when the negative impurity center is in semiconductor with increase of electron velocity at electric field. The current instability appears, i.e. current oscillations in chain takes place in processes of recombination and generation of charge carriers. The ohmic resistance introduced by semiconductor in chain, is negative one in frequency some region. The oscillations of charge carrier and electric field in wave form appear when the processes of recombination and charge carrier generation in semiconductor begin. These waves are absent if they propagate only inside the current oscillation in chain. Such oscillations lead to instable state inside semiconductor and they are called external instability. At definite values of electric field the inner space waves amplify and current oscillations in external chain take place, i.e. (external instability).

The inner and external instabilities in different semiconductors with different impurity centers take place at different values of electric field. Some impurities in semiconductors form the centers which are able to be in several charged states (one-, double- and etc. positive or negative charged ones). Thus, for example, Au atoms in germanium can be one-, double- and triply-charged centers besides neutral one and Cu atoms can be one-, double- and triply-charged centers besides neutral one and etc.

The several energy levels in forbidden band correspond to such impurity centers. These energy levels are situated in different distances from conduction band in forbidden semiconductor region. These deep levels (traps) are able to capture the charge carriers in the dependence on their charge states. The electrical conduction changes in the result of these captures.

In this theoretical work we will investigate the influence of external constant magnetic field on appearance conditions of external instability in definite impurity semiconductors. Let's confirm the values of external electric field and current oscillation frequency at which the external instability appears.

SEMICONDUCTOR MODEL AND MAIN EQUATIONS

We will consider the semiconductor with charge carriers of both signs, i.e. electrons and holes with n_- and n_+ concentrations correspondingly. The negatively charged traps with concentration N_0 are in semiconductor. From them N is concentration of one negatively-charged traps, N_- is concentration of double negatively charged traps [2]

$$\text{i.e.} \quad N_0 = N + N_- \quad (1)$$

$$N_- \ll N, \quad n_{\pm} \ll N, \quad N_- \quad (3)$$

We will consider the current oscillation theory at presence of strong external magnetic field

$$H \gg H_{\pm} = \frac{c}{\mu_{\pm}} \quad (2)$$

The concentration of one- and double-charged traps N, N_- и n_{\pm} satisfy to conduction

The one charged centers capture electrons through Coulomb barrier and emit them through hole barrier, double-charged centers can emit the electrons and capture the holes at thermal excitations.

The concentrations n_{\pm}, N_- and current flow density satisfy to equations (1-3) at presence of electric and magnetic fields [2,3,4]:

$$\begin{aligned} \frac{\partial n_-}{\partial t} + \text{div} \vec{j}_- &= \gamma_-(0)n_{1-}N_- - \gamma_-(E)n_-N = \left(\frac{\partial n_-}{\partial t} \right)_{rek} \\ \frac{\partial n_+}{\partial t} + \text{div} \vec{j}_+ &= \gamma_+(0)n_{1+}N - \gamma_+(E)n_+N_- = \left(\frac{\partial n_+}{\partial t} \right)_{rek} \\ \frac{\partial N_-}{\partial t} &= \left(\frac{\partial n_+}{\partial t} \right)_{rek} - \left(\frac{\partial n_-}{\partial t} \right)_{rek} \quad ; \quad \text{div} J = e \text{div} (\vec{j}_+ - \vec{j}_-) = 0 \end{aligned}$$

$$\begin{aligned} \vec{j}_+ &= n_+\mu_+(E, H)\vec{E} + n_+\mu_{1+}(E, H)[\vec{E}\vec{h}] + n_+\mu_{2+}(E, H)\vec{h}(E, H) - D_+\nabla n_+ - D_{1+}[\vec{\nabla}n_+\vec{h}] - D_{2+}\vec{h}(\vec{\nabla}n_+\vec{h}) \\ \vec{j}_- &= -n_-\mu_-(E, H)\vec{E} + n_-\mu_{1-}(E, H)[\vec{E}\vec{h}] - n_-\mu_{2-}(E, H)\vec{h}(E, H) - D_-\nabla n_- + D_{1-}[\vec{\nabla}n_-\vec{h}] - D_{2-}\vec{h}(\vec{\nabla}n_-\vec{h}) \end{aligned} \quad (4)$$

Here \vec{h} is unit vector in $\vec{H} = H\vec{h}$ magnetic field, $\mu_{\pm}(E, H)$ is ohmic mobility, $\mu_{1\pm}(E, H)$ is $\mu_{2\pm}(E, H)$ Hall mobility, $\mu_{2\pm}(E, H)$ is focusing mobility of holes and electrons, $D_{\pm}, D_{1\pm}, D_{2\pm}$ is corresponding ohmic, Hall and focused diffusion coefficients of charge carriers. We consider the case when carriers have the effective temperature for illumination of lengthy algebraic calculations. Then diffusion coefficients are:

$$D_{\pm} = \frac{T\dot{\gamma}\dot{\phi}\dot{\phi}}{e}\mu_{\pm}, \quad T\dot{\gamma}\dot{\phi}\dot{\phi} = \frac{T}{3}\left(\frac{cE_0}{v_3H}\right)^2 \quad (5)$$

where v_3 is speed of sound, T is lattice temperature in erg.

Besides, we will consider the crystal the sizes of which satisfy to ratio:

$$L_y \ll L_x, \quad L_z \ll L_x \quad (6)$$

$$n_{1-} = \frac{n_-^0 N_0}{N_-^0}; \quad n_{1+} = \frac{n_+^0 N_-^0}{N_0}$$

The external electric field is directed along x axis and magnetic field is directed along z axis.

Let's suppose that $n_{\pm}(\vec{r}, t) = n_{\pm}^0 + \Delta n_{\pm}(r, t)$,

$$N_- = N_-^0 + \Delta N_-(r, t)$$

$$\vec{E}(r, t) = \vec{E}_0 + \vec{\Delta E}(r, t) \quad (7)$$

The inclination of magnetic field from equilibrium value is equal to zero as we consider the longitudinal current oscillations. The sign (0) means the equilibrium value of corresponding values, further it will be omitted.

Let's introduce the following frequencies of capture and emission by equilibrium centers:

$$\nu_- = \gamma_-(E_0)N_0, \quad \nu_+ = \gamma_+(0)N_-^0,$$

$$\nu_+^E = \gamma_+(E_0)N_0$$

And also the combined frequencies:

$$\nu'_- = \gamma_-(E_0)n_-^0 + \gamma_-(0)n_{1-},$$

$$\nu'_+ = \gamma_+(0)n_+^0 + \gamma_+(E_0)n_{1+} \quad (8)$$

Let's designate the numerical factors:

$$\beta_{\pm}^{\gamma} = 2 \frac{d \ln \gamma_{\pm}(E_0)}{d \ln(E_0^2)}; \quad \beta_{\pm}^{\mu} = 1 + \frac{d \ln \mu_{\pm}(E_0)}{d \ln(E_0^2)}$$

$$v_- \gg v'_-, \quad v_+ \gg v'_+$$

Linearizing (4) and taking into consideration (5-7,8) we obtain the vector equation for $\vec{\Delta E}$,

$$\vec{\Delta E} = A\vec{\Delta J} + \vec{B}_1\Delta n_- + \vec{B}_2\Delta n_+ \quad (9)$$

\vec{B}_1 and \vec{B}_2 are constants of current, character frequencies (8) from equilibrium values n_\pm, E, H from numerical values $\beta_\pm^\gamma, \beta_\pm^\mu$. We won't write A, \vec{B}_1, \vec{B}_2 coefficients because they are so cumbersome ones. Let's divide the fluctuations $\Delta n_\pm(r, t), \Delta N_\pm(r, t), \Delta E(r, t)$ in parts which are proportional ones to oscillating current $\Delta J(t)$ in external chain.

$$\Delta n_\pm(r, t) = \Delta n'_\pm e^{i(\vec{k}\vec{r} - \omega t)} + \Delta n''_\pm e^{-i\omega t}$$

$$\Delta N_\pm(r, t) = \Delta N'_\pm e^{i(\vec{k}\vec{r} - \omega t)} + \Delta N''_\pm e^{-i\omega t} \quad (10)$$

$$\Delta E(r, t) = \Delta E' e^{i(\vec{k}\vec{r} - \omega t)} + \Delta E'' e^{-i\omega t}$$

Let's obtain system of heterogeneous equations:

$$\begin{cases} c''_-\Delta n''_- + c''_+\Delta n''_+ = c\Delta J \\ D''_-\Delta n''_- + D''_+\Delta n''_+ = D\Delta J \end{cases} \quad (11)$$

and the system of linear homogeneous equations for $\Delta n'_\pm$:

$$\begin{cases} c'_-\Delta n'_- + c'_+\Delta n'_+ = 0 \\ D'_-\Delta n'_- + D'_+\Delta n'_+ = 0 \end{cases} \quad (12)$$

It is necessary to take into consideration the charge carrier injections on contacts by following way:

$$\Delta n_\pm(0) = \delta_\pm^0 \Delta J,$$

$$\Delta n_\pm(L) = \delta_\pm^L \Delta J \quad (13)$$

where $\delta_\pm^{0,L}$ are injection coefficients of holes and electrons

Substituting (14) into (12) we will definite $\Delta n'_\pm$. After it one can calculate the alternating potential difference on crystal ends and impedance:

$$Z = \frac{\Delta v}{\Delta J}; \quad Z = \frac{1}{\Delta JS'} \int_0^L \Delta E(x, t) dx \quad (14)$$

S is crystal cross-section.

$$Z = \text{Re } z + i \text{Im } z$$

After cumbersome algebraic calculations from (14) we obtain:

$$\begin{aligned} \frac{\text{Re } z}{Z_0} = & \frac{y_2}{\alpha_+} \left\{ 1 - \frac{2n_- v_- \beta_-^\gamma \omega^3}{n_0 \omega_1^4 y \theta} \left[\left(\alpha_- + \frac{v_-^2}{\omega^2} \right) (\cos \varphi - 1) + \frac{v_-}{\omega \alpha_+ \beta_+^\mu} \sin \varphi \right] + \right. \\ & \left. + \frac{2n_+ v_+^E \omega^3 \beta_+^\gamma \alpha_+}{n_0 \omega_1^4 \theta} \left[\frac{\mu_+ (v_+ \omega^2 + v_-^2 v_+^2) \cos \varphi}{\mu_- v_+^E \omega^2 \alpha_- \phi_+^\beta} - \left(\alpha_- + \frac{v_-^2}{\omega^2} \right) \frac{\mu_+}{\mu_-} \left(\frac{1}{\beta_+^\mu} + \frac{v_+}{\omega \beta_+ \mu} \sin \varphi \right) - \frac{evx\delta}{\theta \alpha_+} \frac{\mu_+}{\mu_-} \sin \varphi \right] \right\} \\ \frac{\text{Im } z}{z_0} = & \frac{x}{\theta} \left\{ \frac{3\omega^3 \mu_+}{n_0 \omega_1^4 \alpha_+ \beta_+^\mu \mu_-} \frac{E_0}{E(L_y)} \left(\frac{\mu_- v_3 H}{\mu_+ c E_0} \right)^2 * \right. \\ & * \left[n_+ v_+^E \beta_+^\gamma \left(\alpha_+ + \frac{v_-^2}{\omega^2} \right) - n_- v_- \mu_- \beta_-^\gamma \left(\alpha_- + \frac{v_-^2}{\omega^2} \right) \right] + \frac{ev\delta y}{2\alpha_+} \left(\frac{\mu_+}{\mu_-} \right)^2 \cos \varphi \end{aligned} \quad (15)$$

Here

$$n_0 = n_+ + n_-, \quad v = (\mu_- + \mu_+) E_0, \quad E(L_y) = \frac{Tk_y}{e}; \quad z_0 = \frac{L_x}{\sigma_0 S}$$

$$\omega_1^4 = \omega^4 + v_-^2 v_+^2 + \omega^2 (v_-^2 + v_+^2); \quad \varphi = \frac{\mu_- H}{c \theta}; \quad \sigma_0 = e(n_+ \mu_+ + n_- \mu_-)$$

$$\theta = \frac{L_y L_x v_- \left(n_+ v_+^E \beta_+^\gamma \beta_-^\mu + n_- v_- \beta_-^\gamma \beta_+^\mu \frac{\mu_+}{\mu_-} \right)}{2\pi m_0 v_-^2 (\beta_-^\mu + \beta_+^\mu)} = \left(\frac{E_1}{E_0} \right)^2;$$

$$\delta = \delta_+^0 + \delta_-^0 + \delta_+^L + \delta_-^L, \quad x = \frac{\mu_+ H}{c}; y = \frac{\mu_- H}{c}$$

From (15) it is seen that the definition of E_0 electric field and ω current oscillation frequency is too complex and that's why we will definite E_0 and ω in two limit cases.

HIGH-FREQUENCY CURRENT OSCILLATIONS

$$\text{i.e. } \omega \gg v_+^E, v_-, v_+ \quad (16)$$

The oscillations in external chain appear at $\text{Re } z < 0$ condition. Substituting the positive resistance in (14) one can define the current oscillation frequencies in chain. The equation

$$\frac{\text{Re } z}{z_0} + \frac{R}{z_0} = 0 \quad (17)$$

defines the current oscillation frequencies.

At negative value $\text{Re } z < 0$ JmZ can have the positive or negative sign, i.e. the reactance of capacitive or inductive character. Then the equation

$$\frac{Jmz}{z_0} + \frac{R_1}{z_0} = 0 \quad (18)$$

will define the electric field value at which the current oscillations in chain.

From (18) we easy obtain the following taking into consideration (15):

$$\frac{\omega}{v_-} \left(\frac{E_0^3}{E_3 E_1^2} \cos \varphi - \frac{R_1}{y z_0} \right) = \frac{a E_0}{E(L_y)} (\varphi_+ - \varphi_-) \quad (19)$$

$$a = \left(\frac{Y \mu_- v_3}{\mu_+} \right)^2 \frac{3}{E_1^2}; \quad \varphi_+ = \frac{v_+^E n_+}{v_- n_0} \alpha + \frac{\mu_+}{\mu_-} \beta_+^\gamma;$$

$$\varphi_- = \frac{n_- \beta_-^\gamma \alpha_-}{n_0 \alpha_+}$$

From equation (17) we easily obtain:

$$E_0^2 = E_1^2 \frac{1 + \frac{R \alpha_+}{z_0 y^2}}{\frac{2 n_+ v_+^E \beta_+^\gamma \alpha_+ \alpha_- \mu_+}{n_0 \omega y \mu_- \beta_+ \mu} - \frac{2 n_- v_- \beta_-^\gamma \alpha_- \alpha_+^2}{\omega y n_0 \beta_+ \mu}} \quad (20)$$

$$\cos \varphi = \frac{v_+^E n_+ \beta_+^\gamma \mu_+}{v_- n_- \mu_-} \frac{\alpha_+^2}{\alpha_-} \frac{1}{y} \frac{E_3 E_1^2}{E_0^3}, \quad E_3 = \frac{1}{e \delta \mu_-} \quad (21)$$

For E_0 positiveness

$$\frac{v_+ n_+ \beta_+^\gamma \mu_+}{\mu_-} > v_- n_- \beta_-^\gamma \alpha_- \alpha_+ \quad (22)$$

is required.

Taking into (20-22) from (17) we obtain:

$$\cos \varphi = \frac{1}{\left[1 + \left(\frac{v_+^E}{\omega} \right)^2 U^2 (1-r)^2 \right]^{1/2}} \quad (23)$$

$$U = \frac{E_\delta E_1^2}{E_0^3 Y^2} \frac{2 n_+ \beta_+^\gamma \alpha_+}{n_0} \left(\frac{\mu_+}{\mu_-} \right)^2; \quad r = \frac{v_- n_- \beta_-^\gamma \alpha_- \alpha_+ \mu}{v_+^E n_0 \beta_+^\gamma \mu_+} < 1$$

Finding $\cos \varphi$ from (19) and equate it with (23) we obtain:

$$\omega = v_+^E \frac{n_0}{(n_+ n_-)^{1/2}} \left(\frac{\mu_- v_+^E}{\mu_+ v_- \beta_+^\gamma \alpha_-} \right)^{1/2} \cdot \frac{1}{y^{1/2}} \sim y^{-1/2} \quad (24)$$

$$E_0 = E_1 \left(\frac{n_+ \beta_+^\gamma}{n_-} \frac{v_+^E}{v_-} \frac{\mu_+}{\mu_-} \right)^{1/3} \cdot \frac{1}{y^{1/3}} \sim y^{-1/3} \quad (25)$$

From (24-25) it is seen, that the electric field and current oscillation frequency decrease with increase of external constant magnetic field (at which the external instability appears). However, $\omega \gg v_+^E$ equality should be satisfied at increase of magnetic field. In all conclusions we accept

that $R = Z_0 = \frac{L_x}{\sigma_0 S}$ and we use equality $\mu_- \gg \mu_+$.

LOW-FREQUENCY CURRENT

$$\omega \ll \nu_+^E, \nu_-, \nu_+ \quad (26)$$

Taking into consideration (26) we obtain

$$E_0 = \frac{E_\delta}{E_1 E(L_y)} \left(\frac{\nu_3 \mu_-}{\mu_+^2} \right)^2 \left(\frac{\nu_-}{\nu_+} \right)^3 \frac{3n_0}{n_- \beta_-^\gamma} y^4 \sim y^4 \quad (27)$$

$$\omega = \frac{\nu_+^2}{\nu_-} \left[\frac{E(L_y)}{2E_\delta} \frac{n_- \nu_+ \beta_-^\gamma \mu_-}{6n_+ \nu_+^E \beta_+^\gamma \mu_+} \right]^{2/3} \left(\frac{E_1 \mu_+^2}{\nu_3 \mu_-} \right)^{4/3} y^{-2/3} \sim y^{-2/3} \quad (28)$$

in low-frequency case at $R_1 > 0$ and $R_1 = Z_0$ from (14,15).

From (27-28) it is seen, that electric field increases as $E_0 \sim H^4$ function and frequency decreases as function $\omega \sim H^{-2/3}$ with increase of constant magnetic field.

CONCLUSION

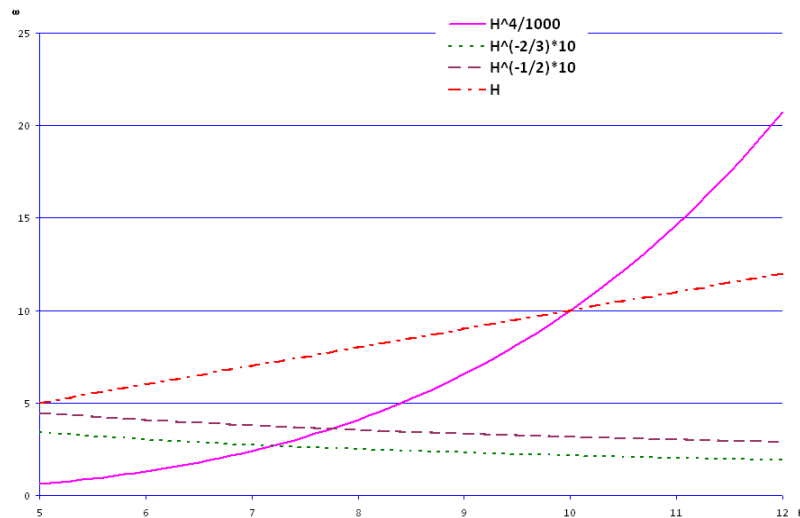
The oscillations with definite frequencies take place in semiconductors with above mentioned impurity centers with two types (electrons and holes) of charge

carriers at presence of electric and magnetic fields $E_0 \perp H_0$. At $\omega \gg \nu_+^E, \nu_-, \nu_+$ the electric field

$E_0 \sim \frac{1}{\sqrt{H}}$ and frequency $\omega \sim \frac{1}{\sqrt[3]{H}}$ depend on magnetic

field correspondingly. At $\omega \ll \nu_+^E, \nu_-, \nu_+$ electric field is as function $E_0 \sim H^4$ and frequency is as $\omega \sim H^{-2/3}$.

Thus, the current oscillation takes place.



- [1] M.I. Iglicin, Э.Г. Pel, L.Ya. Pervova i V.I. Fistul. FTT, 1966, t. 8, vip. 12, str. 3606. c
- [2] V.L. Bon-Burevich, I.N. Zvyagin, A.G. Zvyagin, A.G. Mironov. "Domennaya elektricheskaya neustoychivost v poluprovodnikax". Moskva. «Nauka», 1972, str. 31-35. (In Russian).
- [3] L.E. Gurevich i E.R. Gasanov. FTT, 1969, tom 3, str. 1201-1207. (In Russian).
- [4] E. R. Hasanov, Rasoul Nezhad Hosseyn, Az. Panahov and Ali Ihsan Demirel. "Instability in

- Semiconductors with Deep Traps in the Presence of Strong $(\mu_\pm H \gg C)$ " Advanced Studies in Theoretical Physics. Vol. 5, no. 2011, no. 1, 25-30.
- [5] Ali Ichan Demirel, Eldar Rasuloglu Hasanov, Ekber Zeynalabdinoglu Panahov. "Unstable Waves in Doped Semiconductors and Their Theoretical investigations".
- [6] Y. Y. ü. Fen Bilimleri Enstitüsü Dergisi, Uil 2010, cild 15, sayı 1, sayfa 7-10.

Received: 18.01.2017

ATTRACTORS IN NANO-STRUCTURED LAYERED CRYSTALS

A.Sh. KAKHRAMANOV¹, S.B. BAGIROV²*Baku State University¹**Z.Khalivov str.,23, Baku, Azerbaijan**E-mail: adilqakhramanov@gmail.com**Institute of Physics of ANAS²**AZ -1143, Baku, G.Javid ave., 131*

The impurities accumulate and the quantitative changes take place under influence of intercalation in different $A^V_2B_3^{VI}$ layers: the old bonds are broken and new ones are appeared between its separate layers, even some quintets in $Bi_2Te_3<Cu>$ structures are destroyed and the several nano-objects of fractal character form on their places. These changes lead to instable states, i.e. to bifurcation points. The appeared fluctuations are chaotic ones, some of them damp, only those which form new structures, i.e. attractors attracting the many trajectories of system development and forming the special cone, stay. The nano-islands between $T_e^{(1)} - T_e^{(1)}$ $Bi_2Te_3<Cu>$ layers can be shown in the capacity of its appearance model. If unstable microstructure (curprum in vacancies, between layers and etc) will be in attractor cone, it will evolve to stable state with appearance of many development variants: cluster formation, nano-steps at edge of which the nano-islands form.

Keywords: nano-objects, chaos, dynamics, structures, attractors, cycles, differential equations, stability.

PACS: 61.30.v.; 61.30.Vx.; 67.40.Fd

FRACTALS AND CHAOS IN DYNAMIC SYSTEMS

The determinate equations in systems with dynamic chaos lead to chaotic solutions, i.e. the firstly neighboring trajectories exponentially rapidly diverge in them and instability appears. Moreover, the fractals as geometrical objects can be successfully applied at description of chaotic system trajectories. One can said, that the fractals are the chaos geometrical images.

The structures, changing in time, are defined as dynamic systems. It is clear that chaos is the dynamic fit of the fractal. The chaos describes the states of extreme unpredictability appearing in dynamic system whereas the fractality describes the extreme irregularity inherent to geometric configuration.

Probably, there is no possibility to obtain the math expressions for solution in closed species even the special functions is used.

The dynamic system attractors, in particular, so-called "the strange attractors" are study objects in this direction.

The example that visually demonstrates what is the "chaotic dynamics" is considered in [1]. The following system of differential equations is studied by E.Lorentz with the help of convection flow modeling [1]:

$$\begin{cases} \dot{x} = \frac{dx}{dt} = \sigma(-x + y), \\ \dot{y} = \frac{dy}{dt} = rx - y - xz, \\ \dot{z} = \frac{dz}{dt} = -bz + xy. \end{cases} \quad (1)$$

where σ, r, b are constant positive parameters. The essential dependence on initial conditions that is the main character of chaotic dynamics is inherent to the given system. Here the examples are illustrated what differential equation attractor is. The fractal dimension of concrete differential equation attractors is obtained. Let's consider two examples. The first one is connected with equation system:

$$\begin{cases} \dot{x}_1 = \frac{dx_1}{dt} = -x_1, \\ \dot{x}_2 = \frac{dx_2}{dt} = -2x_2 \end{cases} \quad (2)$$

The general solution of this system is given by formulas:

$$x_1(t) = c_1 * e^{-t}, x_2(t) = c_2 * e^{-2t}, c_1, c_2 = const. \quad (3)$$

If the initial conditions $x_1(0)$ and $x_2(0)$ are given so the trajectory outgoing from this point (i.e. (2) system solution) is given by following formulas:

$$x_1(t) = e^{-t} * x_1(0), x_2(t) = e^{-2t} * x_2(0)$$

Probably, any trajectory at $t \rightarrow +\infty$ strives to (0,0) point. In this simple case we can say that point (0,0) is A system attractor (2) (or solution of (2) system): $A = (0,0)$.

The attractor second example being the limit cycle is: let's the system of two differential equations is given and it has the following form in p, φ polar coordinates on R^2 plane:

$$\dot{p} = p(1-p), \quad (4)$$

$$\dot{\varphi} = 1. \quad (5)$$

From equation (5) it is followed that:

$$\varphi(t) = t + c_1 \quad (6)$$

It is easy to see that the circle is the solution of equation (4).

$$p(t) = 1 \quad (7)$$

Indeed $\dot{p} = 0$ and right part of equation (4) at $p=1$ is transformed in zero:

$$p(1-p^2)/p=1=0.$$

The circles (6), (7) are the solution of systems (4) and (5) and moreover, periodic one with period 2π . Indeed φ polar coordinate has this property: the points with polar coordinates $(1, \phi)$ and $(1, \phi + 2\pi)$ show the one and the same point in the circle $p=1$.

Let's note that if $(p(t), \phi(t))$ are solutions of (4), (5) and $0 < p(t) < 1$ systems then from equation (4) it is followed: $\dot{p}(t) = p(t) * (1 - (p(t))^2) > 0$, i.e. function $p(t)$ increases approximating to value $p=1$ and $(p(t), \phi(t)) = (p(t), t + c_1)$ trajectory does the spiral motion inside circle $p=1$.

If the solution $(p_1(t), \phi(t)) = (p_1(t), t + c_1)$ in some time moment t has $p_1(t) > 1$ then according to equation (4) $\dot{p}_1(t) = p_1(t) * (1 - (p_1(t))^2) < 0$ and $p_1(t)$ decrease with t increase. In this case $(p_1(t), t + c_1)$ curve spirally approaches to $p=1$ circle outside at $t \rightarrow +\infty$.

In [1,2] it is shown that all trajectories of equation system (besides the origin of coordinates $p=0$ which is the fixed point of systems (4) and (5)) strive for $\{p=1\}=A$ circle at $t \rightarrow +\infty$. This is called the limit cycle of systems (4) and (5). Such limit cycle (attracting) is called attractor of systems (4) and (5).

The formation of ordered metallic and semiconductor structures with definite density is understood as self-organization process. The nano-fragments in interlaminar space of $A_2B_3^{VI}$ <impurity> [1-3] crystal can be the example of self-organization example. The formation of interlaminar steps is the also consequence of self-organization. The self organization includes the system interaction able to spontaneous appearance of order in space and in time. It also includes the structural and time order [2].

The appearance of gradation at graphite intercalation by impurities is directly confirmed in electron-microscopic investigations. The co-existence of steps on micro-structural level is shown.

There is necessity in study of nano-fragment morphology forming in interlaminar space of layered crystals by Sb_2Te_3 and Bi_2Te_3 <impurity> type. The fractal particles and nano-meter dimension surfaces are formed as a result of crystallization in interlaminae.

According to above mentioned one can solve the task in revealing of stepped interlaminar structures, nano-islands and other nano-fragments in layered crystals.

The aim of the work is the nano-structurization by impurities and revealing of morphological peculiarities of interlaminar surface (0001) Bi_2Te_3 <impurity> with attracting attractors. The electron-microscopic images are obtained on scanning probe microscope (SPM) by (Комплекс HEKCT mark). X-ray investigations of surface (0001) are carried out on diffractometer by Philips Analytical (XRD).

The appearing steps in $A_2B_3^{VI}$ <In> in increase process play the significant role when intralayer forces significantly exceed the interlaminar ones. The given peculiarities of interlaminar stepped surface can lead to specific dynamics of crystal lattice that should reveal in physical phenomena.

RESULTS AND THEIR DISCUSSION

The physicochemical processes of formation on $A_2B_3^{VI}$ crystal surface (0001) with positions far from

thermodynamic forces and self-organization of fractal structures in medium $T_e^{(1)} - T_e^{(1)}$ (between quintets of crystal structure).

The self-organization processes of impurities of copper and nickel on interlaminar surface (0001) $A_2B_3^{VI}$ <impurity> are investigated with the help of scanning probe microscopy. It is shown that forming impurity surfaces inside $T_e^{(1)} - T_e^{(1)}$ $A_2B_3^{VI}$ <impurity> have the stepped-layered character with nano-islands, nano-bump height forming in process of vertical directed crystallization at step edge are 5-20nm.

The positions of layer-quintets, their atomic defect structure allows to destroy it and form the different types of nano-formations (nano-islands and steps). Moreover, the doping by impurities influences on peculiarities of such crystal electronic properties. The layered character of crystal structure of $A_2B_3^{VI}$ matrix makes possible the shift of easy-diffusing atoms (Cu, Ni, B and other) from indentation center positions where they are in donor states in Van-der-Waals cracks between five-layer packets; here these atoms order and become electrically neutral ones. $T_e^{(1)} - T_e^{(1)}$ distance in $A_2B_3^{VI}$ is bigger than distance of $B_i - T_e^{(1)}$ and $B_i - T_e^{(2)}$.

THE PROCESS OF INTERCALATION AND SELF-INTERCALATION IN $A_2B_3^{VI}$ SYSTEM

Let's consider the atom diffusion along surface (0001) $A_2B_3^{VI}$ <impurity> in direction from "C". The initial energy of atom motion is maximum one. The friction forces with real surface (0001) or collision between moving atoms themselves lead to the fact that atom motion energy transforms into heat energy and disappears. The interlaminar medium $T_e^{(1)} - T_e^{(1)}$ is heated. Moreover, the heating can lead to chemical reactions. For example, at free movement the intercalating atoms disperse the order kinetic energy their movement and transform it in chaotic heat motion of the particles (the process of energy dispersion itself is called dissipation). The systems formed in $T_e^{(1)} - T_e^{(1)}$ $A_2B_3^{VI}$ medium at such gradient processes can be called dissipative ones [1,4]. Here it is said on the atom bond breakage in crystal lattice $T_e^{(1)} - T_e^{(1)}$ $A_2B_3^{VI}$ and the new bonds appear leading to formation of interlaminar nano-structures on the base of impurity super-stoichiometric components. The initial stage can be instable one (bifurcation point).

Thus, copper atom motion from vacant sites of tellurium and bismuth in $T_e^{(1)} - T_e^{(1)}$ Bi_2Te_3 <Cu-In> layers forms the effect of self-intercalation [1] for consideration of their aggregation ways on plane (0001) with nano-island formation. The model of copper atom transition from instable states in bifurcation field (fig.1) is given.

In state far from equilibrium, the very weak fluctuations can step-wise transform the previous structure $A_2B_3^{VI}$ into structure with interlaminar elements with complex destroying structure in whole. Such complex morphological data change in copper atom self-intercalation process from other layers in $T_e^{(1)} - T_e^{(1)}$ layer of very few quantity of copper. Aggregating they form the bigger nano-islands. The considered effects can be considered as the peculiarities of self-organization processes in $A_2B_3^{VI}$ <Cu> systems with formation only interlaminar dissipative nano-islands.

Considering the different fields we see that reconstruction at the presence between the quintets of thermal field take place on surfaces (0001). It is connected with significant inclination and cuprum transition from vacancies and interlaminals in $T_e^{(1)} - T_e^{(1)}$ region. Here the nano-islands (NI), steps, corrugated structures form. Occupying the significant field of this medium, these nano-objects self-organize and transform into different patterns. The self-organization and pattern formation in the form of nano-islands in pattern formation in the form of nano-islands in $\text{Bi}_2\text{Te}_3 <\text{In-Cu}>$ are connected with dissipation conception associating with damping of Cu atom motion from accumulated layers and vacancies (see the arms in fig.1, which show the field “pool”) from which the process of attracting trajectory shows on definite cycle and saves its stability in it in the form of different nano-formations. These cycles can be related to so-called limit ones [4]. According to [4] the any dynamic system has its extraordinary flow, its limit cycle and stay there forever. The own limit cycle in the form of regularly distributed nano-formations in $T_e^{(1)} - T_e^{(1)}$ medium is observed in $\text{Bi}_2\text{Te}_3 <\text{In-Cu}>$ system. And these trajectories can be called not limit cycles but attractors because they like limit cycles attract the trajectories from instable fields (5) and form the geometric fractals in dissipative medium $T_e^{(1)} - T_e^{(1)} A^V_2B_3^{VI} <\text{impurity}>$.

It is considered that dynamic system has the attractor if some right subset A of phase space R^E having the following property: at any point $\sigma(0)$ and enough big t the point $\sigma(t)$ is in small neighborhood of any point belonging to A [1-3].

Each realistic dynamic system achieves the attractor after outflow “enough big” t. The selection result will always coincide with attractors in homogeneous space with concentration gradient. The final result of selection process will correspond to either stable stationary state or periodically changing state family. In some especially occasional situations the non-periodic changes in limits of definite multiple states. The common term that is “attractor” of dynamic system where the stable points can be included, the closed orbits and aperiodic curves [1], is used for characteristics of all these stable and quasi-stable final situations in differential topology. The achievement of the one and the same attractor independently on concrete initial conditions inside the given “pool” is the result of going process.

The density of distribution of such defects as Koch figures, nano-islands, plane breakage (0001) which are steps, is the parameter controlling the achievement of bifurcation point when the dissipative structure with special peculiarities forms that is revealed at processes of intercalation and self-intercalation of Ni, Cu and B impurities.

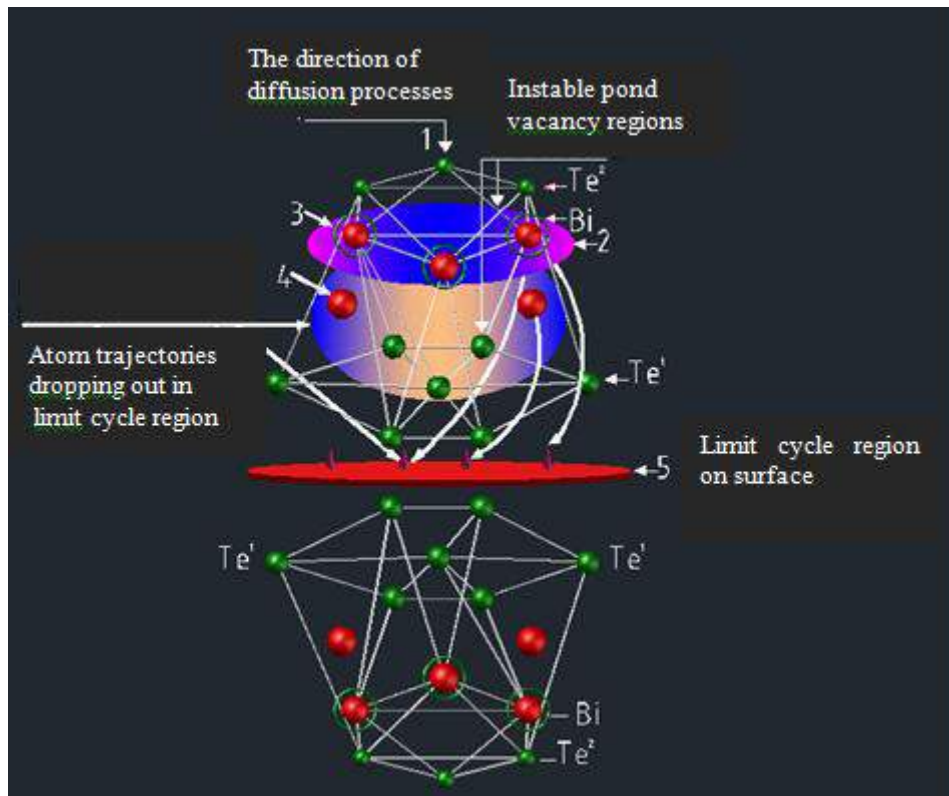


Fig.1. The model of inter-crystalline structure demonstrating the cuprum atom drop-out from B_i layer in which Cu is accumulated. Designations: 1 is Cu diffusion direction at self-intercalation; 2 and 3 are “pool” fields from which Cu atoms diffuse into interlaminar space; 3 are B_i vacancy fields with accumulated Cu atoms; 4 are vacancy fields with cuprum; 5 is interlaminar medium $T_e^{(1)} - T_e^{(1)}$ which is limit cycle field. The places “pools” from which Cu atoms in field (5) are shown by two arms (right at the top) in field (5). The trajectories of atom drop-out into limit cycle fields are shown by arms in left.

- | | |
|---|--|
| [1] <i>B.B. Mandelbrot.</i> Fraktalnaya geometriya prirodi. 1985, s. 327. (In Russian). | [3] <i>S.Sh. Khramanov.</i> Neorganicheskie materiali RAN, 2008, n.1, s.17-25. (In Russian). |
| [2] <i>M. Eygen I P. Shuster.</i> «Giperchikl» M.: Mir, 1982. (In Russian). | [4] <i>G.A. Muchnik.</i> J. Ximiya i jizn, nauka. n.5, 1985, str. 30-35. (In Russian). |

Received: 07.03.2017

HIGGS BOSON PRODUCTION IN NEUTRINO-ELEKTRON SCATTERING

S. K. ABDULLAYEV, M. S. GOJAYEV

Baku State University, AZ-1148, Z.Khalilov, 23, Baku, Azerbaijan

s_abdullayev@mail.ru, m_qocayev@mail.ru

In the framework of Standard Model the processes of scalar Higgs boson production in neutrino-electron scattering has been investigated: $\nu_\mu e^- \rightarrow H \nu_\mu e^-$, $\nu_\mu e^- \rightarrow H \nu_e \mu^-$. The ZZ-fusion and WW-fusion mechanisms are the most important mechanisms for the production of Higgs bosons in neutrino-electron scattering. It is shown that, the process $\nu_\mu e^- \rightarrow H \nu_\mu e^-$ is defined by only two helicity amplitudes: F_{LL} and F_{LR} which describe following reactions: $\nu_\mu e_L^- \rightarrow H \nu_\mu e_L^-$, $\nu_\mu e_R^- \rightarrow H \nu_\mu e_R^-$. The mechanism $WW \rightarrow H$ is defined by one helicity amplitude, which describes the process $\nu_\mu e_L^- \rightarrow H \nu_e \mu_L^-$. We have calculated the cross sections for the helicity processes and detailed numerical results are presented.

Keywords: Standard Model, Higgs boson, left and right coupling constants, helicity amplitudes, Weinberg's parameter, helicity.

PACS: 12.15-y; 12.15 Mm; 14.70 Hp.

1. INTRODUCTION.

The Standard Model (SM) to describe the strong and electroweak interactions between quarks and leptons, is based on the gauge symmetry group $SU(3)_C \times SU(2)_L \times U(1)_Y$. A cornerstone of the SM is the mechanism of spontaneous electroweak symmetry breaking. An $SU(2)$ doublet of complex scalar field is introduced and its neutral component develops a non-zero vacuum expectation value. As a consequence, the electroweak $SU(2)_L \times U(1)_Y$ symmetry is spontaneously broken to the electromagnetic $U_Q(1)$ symmetry. Three of the four degrees of freedom of the doublet scalar field are absorbed by the W^\pm and Z weak vector bosons to form their longitudinal polarizations and to acquire masses. The remaining degree of freedom corresponds to a scalar particle, the Higgs boson.

Some experiments are carried out for the discovery of Higgs boson in different experimental labs. Finally in LHC new information are received concerning the existence of Higgs boson with the mass of 125 GeV [1-5]. So the channels which give rise to Higgs bosons have got more attentions [6-14].

In this work the neutrino-electron scattering are studied for the sake of production of Higgs boson:

$$\nu_\mu + e^- \rightarrow H + \nu_\mu + e^-, \quad (1)$$

$$\nu_\mu + e^- \rightarrow H + \nu_e + \mu^-. \quad (2)$$

2. THE ZZ FUSION MECHANISM

The Feynman diagrams for the Higgs boson production in the ZZ fusion mechanism in the neutrino-electron collisions is shown in the Fig. 1 (the 4-momentum of particles are shown over the diagram).

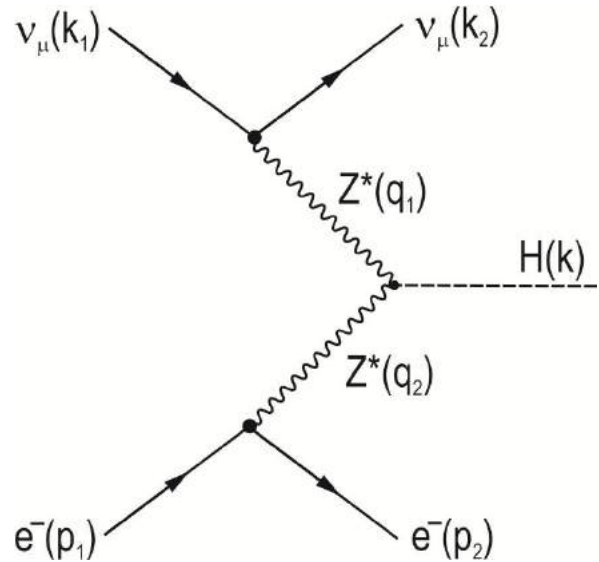


Fig.1. The Feynman diagram for the processes

$$\nu_\mu e^- \rightarrow H \nu_\mu e^-.$$

As we know the lagrangians for interaction of fermions with Z^0 -boson and Z^0 -boson with Higgs boson can be written as follow [15]:

$$L_{\nu_\mu \nu_\mu Z} = \frac{e}{2 \sin \theta_w \cos \theta_w} \frac{1}{2} \bar{\nu}_\mu \gamma_\mu (1 + \gamma_5) \nu_\mu \cdot Z_\mu, \quad (3)$$

$$L_{eeZ} = \frac{e}{2 \sin \theta_w \cos \theta_w} \bar{e} \gamma_\mu [g_L (1 + \gamma_5) + g_R (1 - \gamma_5)] e \cdot Z_\mu, \quad (4)$$

$$L_{ZZH} = \frac{e}{\sin \theta_w \cos \theta_w} M_Z Z_\mu Z_\rho g_{\mu\rho} H(k). \quad (5)$$

Here

$$g_L = -\frac{1}{2} + \sin^2 \theta_w, \quad g_R = \sin^2 \theta_w \quad (6)$$

– are the left and right couplings constants handed

electrons with Z^0 -boson, $x_W = \sin^2 \theta_W$ – is the Weinberg's parameter (θ_W – is the Weinberg's angle), M_Z – is the mass of Z^0 -boson.

According to the lagrangians given in (3)-(5) for the $\nu_\mu + e^- \rightarrow H + \nu_\mu + e^-$ we can write the following transition amplitude:

$$M(\nu_\mu e^- \rightarrow H \nu_\mu e^-) = \left(\frac{e}{2 \sin \theta_W \cos \theta_W} \right)^3 M_Z D_{\mu\rho}(q_1) D_{\rho\nu}(q_2) \bar{u}(k_2) \gamma_\mu (1 + \gamma_5) u(k_1) \times \\ \times \bar{u}(p_2, \lambda_2) \gamma_\nu [g_L(1 + \gamma_5) + g_R(1 - \gamma_5)] u(p_1, \lambda_1) \quad (7)$$

Here

$$D_{\mu\rho}(q_1) = \left(-g_{\mu\rho} + \frac{q_{1\mu} q_{1\rho}}{M_Z^2} \right) \frac{1}{q_1^2 - M_Z^2} \quad (8)$$

– is the propagator of Z^0 -boson, $q_1 = k_1 - k_2$, $q_2 = p_1 - p_2$, λ_1 and λ_2 are the helicities initial and final electrons.

The neutrino and electron weak currents are conserved:

$$(k_1 - k_2)_\mu \bar{u}(k_2) \gamma_\mu (1 + \gamma_5) u(k_1) = 0$$

$$(p_1 - p_2)_\nu \bar{u}(p_2, \lambda_2) \gamma_\nu [g_L(1 + \gamma_5) + g_R(1 - \gamma_5)] u(p_1, \lambda_1) = 0.$$

This will make the amplitude (7) to take a simpler form:

$$M(\nu_\mu e^- \rightarrow H \nu_\mu e^-) = \left(\frac{e}{2 \sin \theta_W \cos \theta_W} \right)^3 M_Z D_1 D_2 [\bar{u}(k_2) \gamma_\mu (1 + \gamma_5) u(k_1) \times \\ \times [\bar{u}(p_2, \lambda_2) \gamma_\mu [g_L(1 + \gamma_5) + g_R(1 - \gamma_5)] u(p_1, \lambda_1)]. \quad (9)$$

Here

$$D_1 = (q_1^2 - M_Z^2)^{-1}, \quad D_2 = (q_2^2 - M_Z^2)^{-2}. \quad (10)$$

As we know the helicity is conserved at high energies. The conservation of helicity imply that initial electron and final electron at the same vertex to have the same helicities: $e_{L(R)}^- \rightarrow e_{L(R)}^-$. Here $e_L^-(e_R^-)$ – is the electron with left (right) helicity. So two helicity amplitudes will correspond to the processes $\nu_\mu + e^- \rightarrow H + \nu_\mu + e^-$: F_{LL} and F_{LR} (first and second indices indicate the initial and final helicities of neutrino and electron). These helicity amplitudes describe the following reactions:

$$\nu_\mu + e_L^- \rightarrow H + \nu_\mu + e_L^-, \quad \nu_\mu + e_R^- \rightarrow H + \nu_\mu + e_R^-$$

and in the framework of SM they are given by expressions

$$F_{LL} = D_1 D_2 g_L, \quad F_{LR} = D_1 D_2 g_R. \quad (11)$$

Let's first calculate the square of amplitude for the spirality process $\nu_\mu + e_L^- \rightarrow H + \nu_\mu + e_L^-$:

$$|M_{LL}|^2 = \left(\frac{e^2}{4x_w(1-x_w)} \right)^3 \cdot M_Z^2 \cdot F_{LL}^2 \cdot T_{\mu\nu}^{(1)} \cdot T_{\mu\nu}^{(2)}. \quad (12)$$

Here $T_{\mu\nu}^{(1)}$ and $T_{\mu\nu}^{(2)}$ are the tensors of neutrino and electron:

$$\begin{aligned} T_{\mu\nu}^{(1)} &= Sp[u(k_2)\bar{u}(k_2)\gamma_\mu(1+\gamma_5)u(k_1)\bar{u}(k_1)\gamma_\nu(1+\gamma_5)] = \\ &= 8[k_{1\mu}k_{2\nu} + k_{2\mu}k_{1\nu} - (k_1 \cdot k_2)g_{\mu\nu} - i\varepsilon_{\mu\nu\rho\sigma}k_{1\rho}k_{2\sigma}], \end{aligned} \quad (10)$$

$$\begin{aligned} T_{\mu\nu}^{(2)} &= Sp[u(p_2, \lambda_2)\bar{u}(p_2, \lambda_2)\gamma_\mu(1+\gamma_5)u(p_1, \lambda_1)\bar{u}(p_1, \lambda_1)\gamma_\nu(1+\gamma_5)] = \\ &= 2(1-\lambda_1)(1-\lambda_2)[p_{1\mu}p_{2\nu} + p_{2\mu}p_{1\nu} - (p_1 \cdot p_2)g_{\mu\nu} - i\varepsilon_{\mu\nu\alpha\beta}p_{1\alpha}p_{2\beta}]. \end{aligned} \quad (11)$$

The product of two tensors $T_{\mu\nu}^{(1)}$ and $T_{\mu\nu}^{(2)}$ is a simple expression:

$$T_{\mu\nu}^{(1)} \cdot T_{\mu\nu}^{(2)} = 2^6 (1-\lambda_1)(1-\lambda_2)(p_1 \cdot k_1)(p_2 \cdot k_2). \quad (12)$$

So, the square amplitude of the process $\nu_\mu + e_L^- \rightarrow H + \nu_\mu + e_L^-$ will be equal to:

$$|M_{LL}|^2 = \left(\frac{e^2}{x_w(1-x_w)} \right)^3 M_Z^2 \cdot F_{LL}^2 \cdot (1-\lambda_1)(1-\lambda_2)(p_1 \cdot k_1)(p_2 \cdot k_2) \quad (13)$$

Analogically we can calculate the square of amplitude for the spirality process $\nu_\mu + e_R^- \rightarrow H + \nu_\mu + e_R^-$:

$$|M_{LR}|^2 = \left(\frac{e^2}{x_w(1-x_w)} \right)^3 M_Z^2 \cdot F_{LR}^2 \cdot (1+\lambda_1)(1+\lambda_2)(p_1 \cdot k_2)(p_2 \cdot k_1). \quad (14)$$

In the center of mass frame the cross section for the helicity processes $\nu_\mu + e_L^- \rightarrow H + \nu_\mu + e_L^-$ is equal to:

$$\sigma_{LL} = \int \frac{|M_{LL}|^2}{16s(2\pi)^5} \delta(p_1 + k_1 - p_2 - k_2 - k) \frac{d\vec{p}_2}{E_2} \frac{d\vec{k}_2}{\omega_2} \frac{d\vec{k}}{E_H}. \quad (15)$$

Here \sqrt{s} is the total energy of neutrino and electron in the center of mass system.

Following Ref. [12] and recalling that the transverse momenta of the scattered particles are small, one may write the four momenta as

$$\begin{aligned} k_1 &= \left(\frac{\sqrt{s}}{2}, \frac{\sqrt{s}}{2}, \vec{0} \right), \quad p_1 = \left(\frac{\sqrt{s}}{2}, -\frac{\sqrt{s}}{2}, \vec{0} \right), \\ k_2 &= \left(x_1 \frac{\sqrt{s}}{2} + \frac{p_{T1}^2}{x_1 \sqrt{s}}, \quad x_1 \frac{\sqrt{s}}{2}, \vec{p}_{T1} \right), \\ p_2 &= \left(x_2 \frac{\sqrt{s}}{2} + \frac{p_{T2}^2}{x_2 \sqrt{s}}, \quad -x_2 \frac{\sqrt{s}}{2}, \vec{p}_{T2} \right). \end{aligned} \quad (16)$$

Neglect terms of the order of $p_{T1}^2/s \ll 1$, $p_{T2}^2/s \ll 1$ in the amplitude squared then immediately obtains for the invariants:

$$(p_1 \cdot k_1)(p_2 \cdot k_2) = (p_1 \cdot k_2)(p_2 \cdot k_1) \approx x_1 x_2 \frac{s^2}{4},$$

$$q_1^2 = (k_1 - k_2)^2 = -2(k_1 \cdot k_2) = -\frac{p_{T1}^2}{x_1},$$

$$q_2^2 = (p_1 - p_2)^2 = -2(p_1 \cdot p_2) = -\frac{p_{T2}^2}{x_2}.$$

Then an amplitude squared for the helicity processes that is simply given by:

$$\begin{aligned} |M_{LL}|^2 &= \left(\frac{e^2}{x_w(1-x_w)} \right)^3 \cdot M_Z^2 \cdot \frac{g_L^2(x_1 x_2)^3 \cdot s^2}{(p_{T1}^2 + x_1 M_Z^2)^2 (p_{T2}^2 + x_2 M_Z^2)^2}, \\ |M_{LR}|^2 &= \left(\frac{e^2}{x_w(1-x_w)} \right)^3 \cdot M_Z^2 \frac{g_R^2(x_1 x_2)^3 \cdot s^2}{(p_{T1}^2 + x_1 M_Z^2)^2 (p_{T2}^2 + x_2 M_Z^2)^2}. \end{aligned} \quad (17)$$

The three-body phase space also simplifies to

$$d\Phi = \frac{d\vec{p}_2}{E_2} \cdot \frac{d\vec{k}_2}{\omega_2} \cdot \frac{d\vec{k}}{E_H} \delta(p_1 + k_1 - p_2 - k_2 - k) = \frac{dx_1}{x_1} \cdot \frac{dx_2}{x_2} d^2 \vec{p}_{T1} d^2 \vec{p}_{T2} \cdot \frac{2}{\hat{s}} \delta((1-x_1)(1-x_2) - r_H) \quad (18)$$

Here $r_H = M_H^2 / s$ and M_H – is the mass of Higgs boson.

The integration on the transverse momenta can there fore be easily done

$$\int \frac{d^2 \vec{p}_{Ti}}{(p_{Ti}^2 + x_i M_Z^2)^2} \approx \pi \int_0^\infty \frac{dp^2}{(p^2 + x_i M_Z^2)} = \frac{\pi}{x_i M_Z^2} \quad (i = 1, 2),$$

with the help of the delta function the integration on x_1 and x_2 are straightforward. One finally obtains for the total helicity cross sections

$$\begin{aligned} \sigma_{LL} &= \frac{1}{4} \cdot \left(\frac{\alpha}{x_w(1-x_w)} \right)^3 \frac{g_L^2}{M_Z^2} f(r_H), \\ \sigma_{LR} &= \frac{1}{4} \cdot \left(\frac{\alpha}{x_w(1-x_w)} \right)^3 \frac{g_R^2}{M_Z^2} f(r_H), \end{aligned} \quad (19)$$

here

$$f(r_H) = (1 + r_H) \ln \frac{1}{r_H} + 2(r_H - 1). \quad (20)$$

The cross section of the process $\nu_\mu + e^- \rightarrow H + \nu_\mu + e^-$ given as follow for the unpolarized electrons

$$\sigma(\nu_\mu e^- \rightarrow H \nu_\mu e^-) = \frac{1}{8} \left(\frac{\alpha}{x_w(1-x_w)} \right)^3 \frac{g_L^2 + g_R^2}{M_Z^2} f(r_H). \quad (21)$$

3. THE W^+W^- FUSION MECHANISM

The process $\nu_\mu + e^- \rightarrow H + \nu_e + \mu^-$ will be due to the W^+W^- -fusion process. The Feynman diagram for these process is shown in Fig. 2.

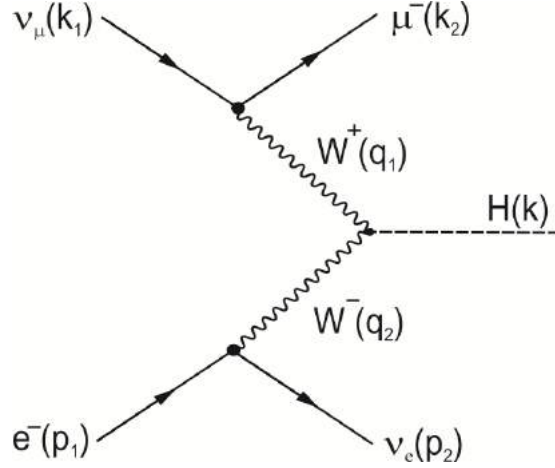


Fig. 2. The Feynman diagram for the processes $\nu_\mu e^- \rightarrow H \nu_e \mu^-$.

In the charge weak neutral current involves only left-handed electrons (muons), so that the process $\nu_\mu + e^- \rightarrow H + \nu_e + \mu^-$ is defined by one helicity amplitude

$$M(\nu_\mu e_L^- \rightarrow H \nu_e \mu_L^-) = \left(\frac{g}{2\sqrt{2}} \right)^2 g M_W \cdot D_3 \cdot D_4 \times \\ \times [\bar{u}(k_2, \lambda_2) \gamma_\mu (1 + \gamma_5) u(k_1)] [\bar{u}(p_2) \gamma_\mu (1 + \gamma_5) u(p_1, \lambda_1)]. \quad (22)$$

here

$$D_3 = (q_1^2 - M_W^2)^{-1}, \quad D_4 = (q_2^2 - M_W^2)^{-1}, \quad (23)$$

M_W is the mass of W -boson, $g = e/\sin \theta_W$ is the coupling constant of the $SU_L(2)$ group.

The square of amplitude (22) is equal to

$$|M(\nu_\mu e_L^- \rightarrow H \nu_e \mu_L^-)|^2 = 4 \left(\frac{e^2}{x_w} \right)^3 M_W^2 D_3^2 D_4^2 (p_1 \cdot k_1)(p_2 \cdot k_2) = \\ = \left(\frac{e^2}{x_w} \right)^3 M_W^2 \cdot \frac{(x_1 x_2)^3 \cdot s^2}{(p_{T1}^2 + x_1 M_W^2)^2 (p_{T2}^2 + x_2 M_W^2)^2}. \quad (24)$$

The total cross section for the process $\nu_\mu + e_L^- \rightarrow H + \nu_e + \mu_L^-$ can be written in the form

$$\sigma(\nu_\mu e^- \rightarrow H \nu_e \mu^-) = \frac{1}{4} \left(\frac{\alpha}{x_w} \right)^3 \cdot \frac{1}{M_W^2} f(r_H) \quad (25)$$

In the case for the unpolarized particles the total cross section given by expression:

$$\sigma(\nu_\mu e^- \rightarrow H \nu_e \mu^-) = \frac{1}{8} \left(\frac{\alpha}{x_w} \right)^3 \cdot \frac{1}{M_W^2} f(r_H). \quad (26)$$

4. CONCLUSION

The total cross sections we obtained for the processes $\nu_\mu e^- \rightarrow H \nu_\mu e^-$, $\nu_\mu e^- \rightarrow H \nu_e \mu^-$. The total cross section for $\nu_\mu e^- \rightarrow H \nu_\mu e^-$ and $\nu_\mu e^- \rightarrow H \nu_e \mu^-$ are displayed in Fig. 3 and 4 as a function of the energy in the center of mass system for $M_H = 125 \text{ GeV}$, $M_Z = 91,1875 \text{ GeV}$, $M_W = 80,425 \text{ GeV}$ and $x_w = 0,232$. One can see that the total production cross sections for the ZZ fusion mechanism is smaller than the cross section for $W^+ W^-$ fusion.

$$\frac{\sigma(ZZ \rightarrow H)}{\sigma(WW \rightarrow H)} \sim 0,2.$$

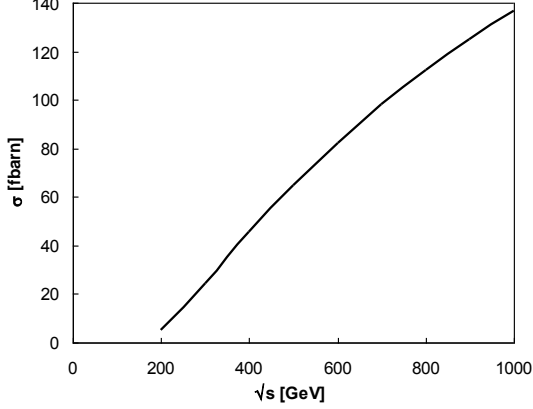


Fig.3. The cross section $\sigma(\nu_\mu e^- \rightarrow H \nu_\mu e^-)$ energy dependence for the $M_H = 125 \text{ GeV}$.

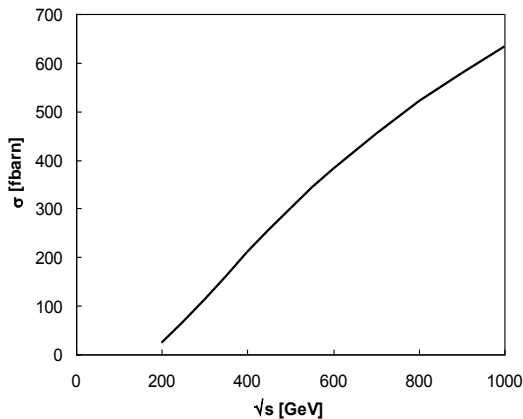


Fig. 4. The cross section $\sigma(\nu_\mu e^- \rightarrow H \nu_e \mu^-)$ energy dependence for the $M_H = 125 \text{ GeV}$.

The cross sections $\sigma(\nu_\mu e^- \rightarrow H \nu_\mu e^-)$ and $\sigma(\nu_\mu e^- \rightarrow H \nu_e \mu^-)$ are shown in Fig. 5 and 6 as a function M_H for the energy $\sqrt{s} = 500 \text{ GeV}$. By increasing the Higgs boson mass the cross section will be decreased.

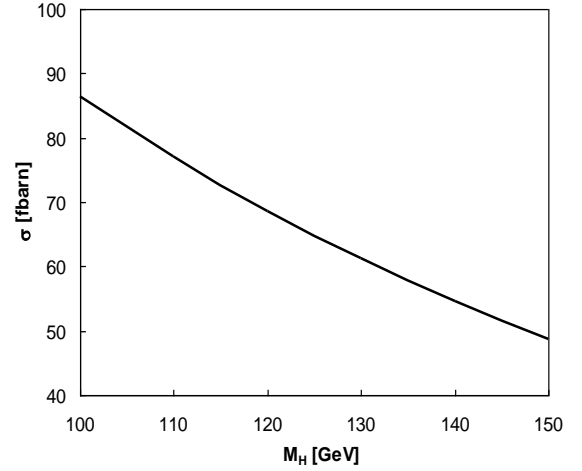


Fig. 5. The cross section $\sigma(\nu_\mu e^- \rightarrow H \nu_\mu e^-)$ as a function of M_H .

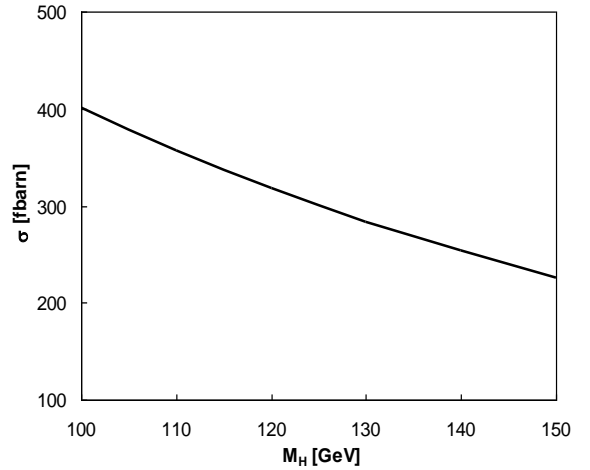


Fig. 6. The cross section $\sigma(\nu_\mu e^- \rightarrow H \nu_e \mu^-)$ as a function of M_H .

- [1] ATLAS Collaboration. Observation of a new particle in the search for the Standard Model Higgs boson with the ATLAS detector at the LHC. Phys. Letters, 2012, B716, p. 1-29.
- [2] CMS Collaboration. Observation of a new boson at mass of 125 GeV with the CMS experiment at the LHC. Phys. Letters, 2012, B716, p.30-60.
- [3] V.A. Rubakov. Uspexi fizicheskix nauk. 2012, tom 182, №10, s. 1017-1025 (In Russian).
- [4] A.V. Lanev. UFN, 2014, t.184, №9, s.996-1004 (In Russian).
- [5] D.I. Kazakov. UFN, 2014,t.184, №9, s.1004-1017 (In Russian).
- [6] A. Djouadi. The Anatomy of Electro-Weak Symmetry Breaking. Tome I: The Higgs boson in the Standard Model. arXiv: hep-ph/0503172v2, 3 May, 2005
- [7] V.M. Emelyanov. Standartnaya model I ee rasshirenie. M.: Fizmatlit, 2007, 584s. (In Russian).
- [8] P. Langacker. The Standard Model and Beyond. CRC Press, 2010, 635p.
- [9] A.A. Anselm, N.Q. Uralchev, V.A. Xoze. Xiqgovskie chastich; UFN, 1985, t.145, №2, s.185-223. (In Russian).
- [10] A.I. Vaynshteyn, M.A. Zaxarov, M.A. Shifman. Xiqgovskie chastich; UFN, 1980, t.131, №8, s.537-575. (In Russian).
- [11] S.K. Abdullayev, L.A. Aqamalieva, M.Sh. Qodjaev, F.A. Saddix. Qruzinskiy elektronniy nauchniy jurnal Fizika. 2015, №1(13), s.36-55 (In Russian).
- [12] S.K. Abdullayev, L.A. Aqamalieva, M.Sh. Qodjaev, F.A. Saddix. Qruzinskiy elektronniy nauchniy jurnal Fizika. 2015, №2(14), s.28-40 (In Russian).
- [13] S.K. Abdullayev, M.Sh. Qodjaev, F.A. Saddix. Kanali raspada standartnoqo xiqts bozona. Vestnik Moskovskoqo Universiteta. 2017, №.., s (v pechatı) (In Russian).
- [14] E.E. Booss. UFN, 2014, t.184, №9, s.985-996. (In Russian).
- [15] S.Q. Abdullayev. Lepton-lepton və lepton-hadron qarşılıqlı təsirlərində zəif cərəyan effektləri (I hissə), Bakı, «AM 965 MMC», 2012, 484 səh.

Received: 15.03.2017

MATHEMATICAL MODELLING OF THE ELECTRON STRUCTURE OF SiO₂ NANOPARTICLE

A.G. GASANOV, A.A. BAYRAMOV, E.G. HASHIMOV

War College of Armed Forces of the Azerbaijan Republic

E-mail: hasanovarzuman@hotmail.com;

azad.bayramov@yahoo.com; hasimovel@gmail.com

The electronic structure of (SiO₂)_n nanoparticles were investigated by non-empirical method. This method is a variant of the molecular orbitals method. Molecular orbitals are represented as a linear combination of atomic orbital's of the atoms of the nanoparticle. The numerical values of the unknown coefficients of the linear combination are found by solution of equations of molecular orbitals. The orbital energies, potential ionization, the total electronic energy of (SiO₂)_n nanoparticles were calculated. The results show that in case of $n=1, 2, 3, 4, 6$ then the (SiO₂)_n nanoparticles are dialectical, and in case of $n=7, 8, 10$ и 12 the ones are semi conductive hard, nucleophile and stabile materials.

Key words: computer modeling, nanotechnology, quantum mechanical calculations, non-empirical method.

PACS: 07.05.Tp, 81.07.-b, 03.67.Lx.

INTRODUCTION

(SiO₂)_n nanoparticles due to its properties have been applied on wide range [1-4], for example, in electronic industry in planar processes for forming electron plates, in military industry for making hard guard covers etc. So, it is very important to investigate of the electron structure of (SiO₂)_n nanoparticle by quantum mechanics method.

From the point of view of electrophysical properties as opposed to volumetric materials the quantum effects play much part in nanosystems, because wave functions have hard constraints. In this time the electronic structure of nanoparticles are qualitatively similar to electronic structure of molecules and is consisted of the assembly of discrete states.

Usually, the nanoparticles' electronic structure is differed from the volumetric materials' one, especially near of the range of Fermi level. The metal conductivity materials can turn into the dielectric and semiconductive materials, and the dielectrics can turn into the metals.

During modelling of nanoparticles and nanosystems, first of all, its equilibrium atom structure and form are determined. At this stage it is determined how change of the form and the structure when the volume of nanoparticles is changed. If we know this, then we can simulate an assemblage of nanoparticles and nanosystems. The common method of this procedure is calculation of total energy of the system and searching its minimum.

In our last works [5-8] we have constructed theoretical models of the electronic structures of nanoparticles and nanocomposites.

In [5] the theoretical visual model was constructed for the silver nanoparticles and their nano-composites. These models were investigated by Hartree-Fock-Roothan method. The results of the calculations show that the silver nanoparticles and their PP+Ag₅ and PVDF+Ag₅ nano-composites are tough, nucleophile and stable dielectric materials.

In [6] the electronic structure of the cadmium sulfur CdS nanoparticles were investigated by semi-empirical Wolfsberg – Helmholtz method. Molecular orbitals are represented as a linear combination of valence atomic

orbitals of the atoms of the nanoparticle. The orbital energies, potential ionization, the total electronic energy and effective charge of atoms of cadmium sulfur nanoparticles were calculated.

By the same method in [7] for Au and in [8] for Ag nanoparticles the electronic structures were investigated. Here, the calculations have been carried out on the basis of Slater functions.

Now, in given paper the electronic structure and properties of the (SiO₂)_n nanoparticle were investigated by non-empirical method [9]. It is implied that this method is most informative and so it is most suitable.

THEORETICAL METHODOLOGY

It is known, that the structure and properties of nanoparticles are determined by number and size of atoms inside one [3]. There are various methods for determination of atom number. Knowing the covalent radius of Si and O atoms ($r_{Si}=0,111$ nm, $r_O=0,073$ nm – see periodic table [10]) it is possible to determine the approximate radius of sphere where there is one Si and two O atoms. For this, let us use theoretical models of SiO₂ molecule and (SiO₂)_n nanoparticle (fig. 1).

The radius r_h of adopted as sphere form of SiO₂ molecule is determined from $\triangle ACD$ triangle (or $\triangle ABC$)

$$r_h = AC/2 \quad (\text{or } r_h = AB/2)$$

In this right triangle we have

$$AC = \sqrt{AD^2 + CD^2}$$

and

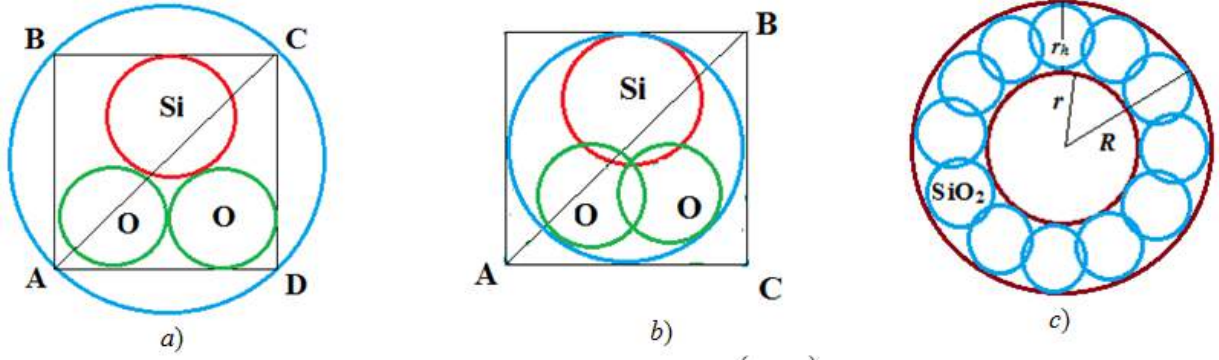
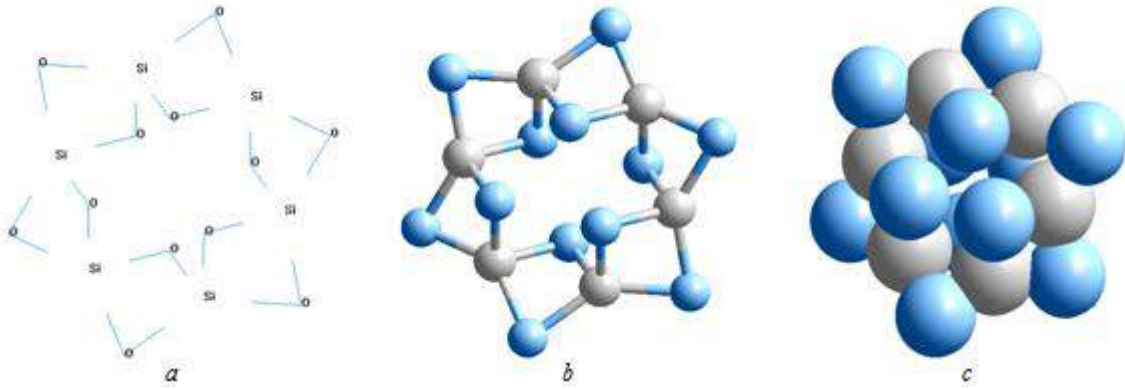
$$AD = 4r_O$$

and

$$CD \approx 2(r_{Si} + r_O)$$

$$\text{So, } r_h \approx 0,24 \text{ nm.}$$

The number of atom in the nanoparticle can be calculated by approximate formula [6]


 Fig. 1. Theoretical models of SiO₂ molecule (a and b) and (SiO₂)_n nanoparticle (c).

 Fig. 2. Various forms models of (SiO₂)_n nanoparticle (n=6, N=18): lines (a), lines and spheres (b), spheres (c).

$$n = \frac{R^3 - r^3}{r_h^3}$$

Here, r is inter radius of nanoparticle.

If we accept that $r \approx 0$, then

$$n = \left(\frac{R}{r_h} \right)^3$$

Here, R is a radius of adopted as sphere form of (SiO₂)_n nanoparticle.

If $R=0,43$ nm then we have $n=6$. The total number of silicium and oxygen atoms is $N=18$. Then, the theoretical models of (SiO₂)_n nanoparticle can be constructed by various forms in depended on n (figure 2.). The non-empirical or Hartree-Fock-Roothan (HFR) method is a one of the quantum-mechanical methods used for investigation of quantum levels of nanosystems [5,11,12]. The main idea of this method is that inside a nanosystem the nanoparticle interaction with each other is substituted for some $V(r)$ potential. So, the quantum-mechanical multiparticles' task is substituted for one particle's task and below HFR equations are used for investigation of quantum levels of nanosystems:

$$\sum_{q=1}^m (F_{i,pq} - \varepsilon_i S_{pq}) c_{qi} = 0, \quad (p = \overline{1, m}) \quad (1)$$

here

$$F_{i,pq} = f_i H_{pq} + \sum_{jkl} \sum_{rs} c_{rk}^* c_{sl} (2A_{ij,kl} J_{prqs} - B_{ij,kl} J_{prsq})$$

$$S_{pq} = \int \chi_p \chi_q dV$$

Here: ε_i is orbital energy of the i electron, f_i is a degree of fill of the i level by electrons, c_{qi} are unknown factors, χ_p

are basis functions, S_{pq} is overlapping matrix, H_{pq} are one electron matrix elements of Hamilton operator, J_{prqs} and

J_{pqrs} are two electron matrix elements, $A_{ij,kl}$ and $B_{ij,kl}$ are the given 4 dimensional matrixes. (1) equations are called

HFR ones. The total energy of system is calculated by next formula:

$$E = 2 \sum_{ipq} c_{pi}^* c_{qi} f_i H_{pq} + \sum_{ijkl} \sum_{pqrs} c_{pi}^* c_{rk}^* c_{qj} c_{sl} (2A_{ij,kl} J_{pqrs} - B_{ij,kl} J_{pqrs})$$

For find of unknown factors c_{qi} we should solve non-linear uniform algebraic equations (1). In this time we adopt that the basis functions χ_p are known. These functions describe electron's states inside the atom. And so, we adopt that the numerical values of S_{pq} , H_{pq} , J_{pqrs} , J_{pqrs} , $A_{ij,kl}$ and $B_{ij,kl}$ matrix elements in these equations are known. $F_{i,pq}$ quantities are non-linearly depended on c_{qi} unknown quantities and so, (1) equations' system is a non-linear algebraic one and below these equations' system can be written as matrix form:

$$F \cdot C = E \cdot S \cdot C \quad (2)$$

Here: E – is a vector of orbital energy of electrons, S is an overlapping matrix, C is a matrix of unknown factors, F is a Fock matrix depended on the matrix elements of unknown C factors. (2) is an equation of generalized eigenvalues.

Using unitary transformation the generalized eigenvalues equation (2) can be transformed to common eigenvalues equation. For this we use V unitary matrix which transforms S matrix to I unit matrix

$$V^T \cdot S \cdot V = I$$

Then

$$X = V^{-1} \cdot C$$

and

$$F' = V^T \cdot F \cdot V$$

Finally, we obtain eigenvalues equation

$$F' \cdot X = E \cdot X \quad (3)$$

For solving equation (3) we use method of F' Fock matrix diagonalization. As result, we determine the values of ε_i orbital energies and c_{qi} factors. Now, knowing calculated ε_i and c_{qi} values we can determine total electron energy of system, ionization potential, effective charge of atoms etc.

Should be note, that non-empirical method is one of the molecular orbitals (MO) methods. It is adopted that in MO method each electron in molecule moves in certain effective field created by atoms and electrons of molecules not depended on other electrons. The electron's state in molecule is described by one electron wave function (molecule orbital). These functions are multicentered ones. That is, its expressions include a distance of electrons from nucleuse of various atoms.

There are various variants of seaching of the molecule's orbites. The MO LCAO method [13,14,15] of

the seaching of U_i molecule orbits as the atom's orbits linear combination is one of them:

$$U_i = \sum_{q=1}^m c_{qi} \chi_q \quad (4)$$

Here: c_{qi} are unknown factors, χ_q are atoms' orbits as basis functions.

In (4) equation Gauss functions were used as χ_q atom's orbits [9]. Orbits energies ε_i were calculated for each n . For $n=6$ state the orbits energies are presented in table 1.

By using ε_i values $(\text{SiO}_2)_n$ nanoparticles total electron energy and ionization potential can be calculated, mechanical, electrical, magnetical properties etc. can be investigated.

For calculations we have used Mathcad and HyperChem 7.5 programs (free version).

CALCULATIONS FOR $(\text{SiO}_2)_n$ NANOPARTICLE AND ANALYSIS

The results of calculations of the orbits energies, ionization potential and total electron energies of $(\text{SiO}_2)_n$ nanoparticle are presented in table 2. The electrons of $(\text{SiO}_2)_n$ nanoparticle are located on two-two levels beginning on the lowest energy level. The capture by electrons upperst molecule's orbits energy $\varepsilon_{\text{HOMO}}$ and lowest empty molecule's orbit energy $\varepsilon_{\text{LUMO}}$ have been determined. Ionization potential of nanoparticle $I_p = -\varepsilon_{\text{HOMO}}$ and band-gap energy $E_g = \varepsilon_{\text{LUMO}} - \varepsilon_{\text{HOMO}}$ have been calculated. As seen from table 2, for $(\text{SiO}_2)_n$ nanoparticle the minimum value of stabilization parameter is obtained at $n=6$. In this case, the value of band-gap energy is $E_g = 12,890254 \text{ eV}$. At $n=6$ it indicates that $(\text{SiO}_2)_n$ nanoparticle is a dielectric material. From scientific publications there is $E_g = 8-9 \text{ eV}$ for SiO_2 [16].

The solidity and radiated photon wave lenght of nanoparticle can be calculated by below formules, respectively [5-8]

$$\eta = \frac{1}{2} E_g \text{ and } \lambda = \frac{c \cdot h}{1,6 \cdot E_g} \cdot 10^{28} \text{ nm}.$$

Here: h is Planck's constant, c is a light speed in vacuum. When $\eta < 1 \text{ eV}$ the material is soft, when $\eta > 1 \text{ eV}$ the material is solid. If $n=6$ then $\eta > 1 \text{ eV}$ and $(\text{SiO}_2)_n$ nanoparticle is a solid dielectric material. $(\text{SiO}_2)_n$ nanoparticle is nucleophil because the

lowest empty molecule orbit energy has a positive sign.
The stability of (SiO₂)_n nanoparticle is calculated by below formula [5-8]

$$\Delta E((\text{SiO}_2)_n) = E_{(\text{SiO}_2)_n} - n \cdot (E_{\text{Si}} + 2E_{\text{O}})$$

If $\Delta E((\text{SiO}_2)_n) > 0$ then the material is non-stable, if $\Delta E((\text{SiO}_2)_n) < 0$ then the material is stable.
(SiO₂)_n nanoparticles are non-stable at n = 4, 9, 11 and are stable at n=1, 2, 3, 5, 6, 7, 8, 10, 12. The results are presented in table 2.

Table 1.

The values of *i* orbits energies (eV) for (SiO₂)₆ nanoparticle

<i>i</i> = 1,2,...,30	<i>i</i> = 31,32,...,60	<i>i</i> = 61,62,...,90	<i>i</i> = 91,92,...,114
-1852.60252	-111.224844	-14.497279	5.449863
-1852.60231	-111.201595	-13.196862	6.559509
-1852.60123	-111.200924	-13.196764	6.560208
-1852.60003	-111.172931	-12.894042	7.942687
-1852.59893	-111.172104	-12.891976	7.944644
-1852.59815	-111.161577	-12.684754	8.507430
-550.261493	-111.150486	-12.398353	8.706767
-550.260576	-111.144948	-12.396422	9.576916
-550.258934	-111.144168	-12.181360	10.545444
-550.258179	-111.122919	-11.187507	10.548156
-550.257061	-111.121919	-11.186590	10.924087
-550.255843	-111.112633	-10.663999	10.928117
-548.973874	-35.017569	-10.567299	12.064183
-548.972954	-34.096239	-10.478238	12.064934
-548.968453	-34.093681	-10.224824	12.751561
-548.967345	-33.272679	-10.222495	12.902745
-548.964483	-33.271238	-9.830077	12.906865
-548.958380	-33.060528	-9.828017	13.089263
-164.977808	-32.424266	-9.732331	16.800189
-164.965241	-32.421465	-9.730517	16.804941
-164.964113	-31.884290	-9.540998	17.134486
-164.942126	-31.881379	-9.287795	18.512019
-164.941026	-31.659088	-9.252553	18.516079
-164.930328	-31.655735	-8.935980	19.950982
-111.304568	-17.167922	-8.932199	
-111.283740	-17.165280	-8.500290	
-111.282658	-16.698655	-8.194362	
-111.250171	-16.695127	-8.190613	
-111.249198	-16.662022	-7.444088	
-111.228622	-16.462190	-7.440391	

Table 2.

The results obtained for (SiO₂)_n nanoparticle

N	Objekt	\mathcal{E}_{HOMO}	\mathcal{E}_{LUMO}	Total energy <i>E</i> (a.u.)	Stable parameter ΔE (a.u.)	Ionizing potential <i>I_p</i> (eV)	Band-gap energy <i>E_g</i> (eV)	Solid parameter η (eV)	Photon wavelength λ (nm)
1	SiO2	-7.46791	5.536341	-433.3548767	-1.642570853	7.46791	13.004251	6.5021255	95.594
2	(SiO2) ₂	-5.447256	1.681954	-866.4987541	-0.98804751	5.447256	7.12921	3.564605	174.371
3	(SiO2) ₃	-6.219263	0.466485	-1299.908631	-1.642570853	6.219263	6.685748	3.342874	185.937
4	(SiO2) ₄	-3.576335	3.535457	-1730.039457	0.981955843	3.576335	7.111792	3.555896	174.798
5	(SiO2) ₅	-2.687114	1.931155	-2166.265703	-2.488936726	2.687114	4.618269	2.3091345	269.176
6	(SiO2) ₆	-7.440391	5.449863	-2600.645508	-4.113388277	7.440391	12.890254	6.445127	96.439
7	(SiO2) ₇	-0.812659	2.463377	-3033.426918	-4.139445511	0.812659	3.276036	1.638018	379.460
8	(SiO2) ₈	-3.396007	1.618684	-3463.449217	-1.40639056	3.396007	5.014691	2.5073455	247.897
9	(SiO2) ₉	-2.787062	2.885106	-3893.920946	0.877233848	2.787062	5.672168	2.836084	219.162
10	(SiO2) ₁₀	-2.040018	2.950686	-4330.165495	-2.611962388	2.040018	4.990704	2.495352	249.088
11	(SiO2) ₁₁	-3.336001	2.489439	-4757.267161	3.041725181	3.336001	5.82544	2.91272	213.396
12	(SiO2) ₁₂	-1.228955	2.587575	-5200.237772	-7.17353312	1.228955	3.81653	1.908265	325.721

CONCLUSION

So, the electronic structure of the $(\text{SiO}_2)_n$ nanoparticles were investigated by non-empirical method. The results of calculations show that $(\text{SiO}_2)_n$ nanoparticle is solid, nucleophil, dielectric material at

$n=1, 2, 3, 4, 6$ and is solid, nucleophil, semiconductive material at $n=5, 7, 8, 9, 10, 11, 12$. $(\text{SiO}_2)_n$ nanoparticles are non-stable at $n = 4, 9, 11$ and are stable at $n=1, 2, 3, 5, 6, 7, 8, 10, 12$. These materials can be applied for making various electronic plates and for military covering materials.

-
- [1] Yu.E. Burunkova, I.Yu. Denisyuk, S.A. Semyina. "Optic journal", 79, 2, 2012. 67-71 p.
 - [2] A.V. Nomoev. Pisma JTF, 2012, v.38, is. 10, 35-42 p.
 - [3] Chandra Dhakal. Computational modeling of amorphous SiO_2 nanoparticles and their electronic structure calculation. A master thesis in Physics. Kansas City, Missouri 2015, 76 p.
 - [4] Wang Yao, Gu Guangsheng, Wei Fei, Wu Jun. Fluidization and agglomerate structure of SiO_2 nanoparticles. Powder Technology. 124 (2002). 152– 159 pp.
 - [5] F.H. Paşayev, A.Q. Həsənov. Bakı Universitetinin Xəbərləri. Fizika-riyaziyyat elmləri seriyası 2013, №1, s.146-156.
 - [6] M.A. Ramazanov, F.G. Pashaev, A.G. Gasanov, A.M. Maharramov, A.T. Mahmood. The quantum mechanical study of cadmium sulfur nanoparticles in basis of sto's Chalcogenide Letters, V11(7), 359-364. (2014).
 - [7] F.G. Pashaev, A.G. Gasanov and A.T. Mahmood. The Study of Gold Nanoparticles in basis of Slater Functions J. Nano. Adv. Mat., V 2(1), 35-41. (2014).
 - [8] A.M. Maharramov, M.A. Ramazanov, A.G. Gasanov, F.G. Pashaev. The Study of Silver Nanoparticles in Basis of Slater Functions. Physical Science International Journal. 10(3): 1-6, 2016.
 - [9] V.I. Minkin, B.Y. Simkin, R.M. Minyaev. Theory of structure of molecule. Rostov at Don, Feniks, (2010).
 - [10] A.A. Bayramov, E.X. Məmmədov. Atom and nucleus Physics. AF War College. Military publishing, Baku, 2016, 232 p.
 - [11] A. Messia. Quantum mechanics. M.: Nauka, 1979. v. 2. p. 254-290.
 - [12] S.K. Ignatov. Quantum-chemical modeling of molecular structure, physical-chemical properties and reaction possibility. Part 1. Nijniynovgorod State University. Nijniy Novgorod. 2006, 82 p.
 - [13] A.M. Magerramov, R.A. Alieva, F.G. Pashaev, A.G. Gasanov etc. Journal of Dyes and Pigments, V 85, Issues 1-2, 1 (2010) pp.1-6.
 - [14] R.A. Alieva, F.G. Pashaev, A.G. Gasanov, K.T. Mahmudov. Russian Journal of Inorganic Chemistry, 2009, Vol. 54, No. 9, pp. 1407–1411.
 - [15] A.S. Fedorov, P.B. Sorokin etc. Modeling of the properties of the electronic structure of some carbon and non-carbon nanoclusters and their interaction with light elements. Novosibirsk, (2006).
 - [16] G.Z. Victor. Computer modeling of nanoparticles and nanosystems. Material Sciences Institute. ChScC RAN, 2006, 137 p.

Receviad: 10.01.2017

THERMAL AND ELECTRICAL PROPERTIES OF GaSb-CrSb EUTECTIC COMPOSITE

M.V. KAZIMOV

*Institute of Physics of the Azerbaijan National Academy of Sciences;**E-mail: mobilkazimov@gmail.com*

In GaSb-CrSb eutectic composite, the electrical and thermal conductivity, thermoelectric power and Hall coefficients were investigated in a wide temperature range. The heat transfer mechanisms have been discussed in the framework Callaway model. The thermal conductivity calculated with taken into account the role of the charge carriers transfer, point defects, three-phonon normal and three-phonon umklapp processes and the mechanism of resonance transfer of ionization energy.

Keywords: Eutectic composite, XRD, SEM and EDX analysis, thermal and electrical conductivity, thermoelectrical power, Hall coefficient

PACS: 536.21

1. INTRODUCTION

Microelectronics development depends on novel with controlled properties materials. For this purpose the eutectic composites based on III-V compounds and 3d-metals, where the metallic phase with needle-shaped are form and oriented parallel in the matrix, may be used for galvanomagnetic, thermomagnetic, photothermomagnetic and strain sensitive translators [1-3]. The advantage of such compositions is the combination of semiconductor and metal properties. GaSb-CrSb eutectic composite, as one of heterogeneous semiconductors, consists from diamond-like GaSb and compound CrSb with hexagonal structure. The NiAs type CrSb compound is antiferromagnetic below about 700K, where the magnetic moments of Cr ions are directed along the c-axis, aligned ferromagnetically in the c-plane, and antiferromagnetically in the adjacent c-planes [4]. From this point of view GaSb-CrSb eutectic composite, as deluted magnetic semiconductor may be one of the the promising material for spintronic devices [5, 6].

Previously, by XRD analysis it was confirmed that GaSb-CrSb composite has a two-phase structure [7, 8]. Heat flow and heat capacity studies have been made in the 293-1273K temperature range, and enthalpy of fusion and specific heat were determined. The initial and final points of melting temperature are determined as 943K and 965K, respectively [8].

The present work is focused on the electron micrographic analyses, electrical and thermal conductivity of GaSb-CrSb composite.

2. EXPERIMENTAL

GaSb-CrSb eutectic composites were prepared by using the vertical Bridgman method. The rate of the crystallization front was about (0.3÷0.6) mm/min. XRD intensity data were collected on an Advance-D8 diffractometer using CuK α radiation. A Zeiss SIGMA Field Emission Scanning Electron Microscope (FESM), equipped "Oxford EDS" и "HKL EBSD", were used to characterize the morphology of the specimens and to obtain qualitative information on the elemental composition of the samples, respectively. Samples for electric measurement were prepared in a parallelepiped form with size (2×4×10) cm³. On the both lateral sides of the samples, four contact probes were attached to measure the electrical conductivity (σ), thermal power (α) and Hall

coefficient (R) using the compensation method, and the thermal conductivity (K) was measured by the absolute stationary heat flow method.

3. RESULTS AND DISCUSSION

Diffraction patterns of GaSb-CrSb eutectic composite are shown in Fig. 1. These figures also show data on the diffraction patterns for GaSb and CrSb compounds. Analysis of XRD spectra confirmed that this system is diphasic: the most intense peaks corresponding to the (111), (200), (220), (311), (222), (400), (331), (420), and (422) Muller index are identical to the GaSb matrix, while the weak peaks found at $2\theta = 30^\circ, 44.08^\circ, 52.12^\circ$, and 54.13° coincide with the CrSb lines having a hexagonal structure with lattice parameters of $a = 4.121$, $c = 5.467$, $c/a = 1.327$, and the P63/mmc space group.

Based on SEM examinations (Figs.2), the needle-shaped metallic inclusions with a diameter of about 0.9-1.6 μm , a length of 20÷50 μm and a density of $\sim 6 \times 10^4 \text{ mm}^{-2}$ are uniformly and parallel distributed in the GaSb matrix. It was found that the matrix contains Ga = 36.1wt%, Sb = 63.9 wt% (Fig.3, spectrum 1), the inclusion are contained Cr = 27.8 wt%, Sb = 72.2 wt% (Fig.3, spectrum2). The data correspond to the stoichiometric composition of the matrix and inclusions. Fig.4 shows elemental maps of Cr, Ga and Sb from the cross sections along the lateral direction of the needle phases, respectively. In the specific map, the colours red, blue and green indicate Sb (L), Cr (K) and Ga (K), respectively and black colour indicates the absence of this element.

The temperature dependence of the Hall coefficient $R(T)$ and electrical conductivity $\sigma(T)$ at the different mutual directions of current (I), magnetic field (B), and crystallization direction (x) have been measured. The Hall coefficient drops along the sample in the case of $I \parallel x \perp B$ due to the short-circuiting by inclusions of the current through the sample and the Hall voltage one in the case of $I \perp x \perp B$ has a minimum value [9], because, the Hall coefficient have been measured in the case of $I \perp x \parallel B$, where there is no shorting of any current or Hall potential. It is evident from Fig. 5 that the Hall coefficient remains unchanged in a temperature range of 80÷475 K. The sign of the Hall coefficient changes at temperatures between 490 and 515 K (the inversion charge for GaSb is take place at 560 K).

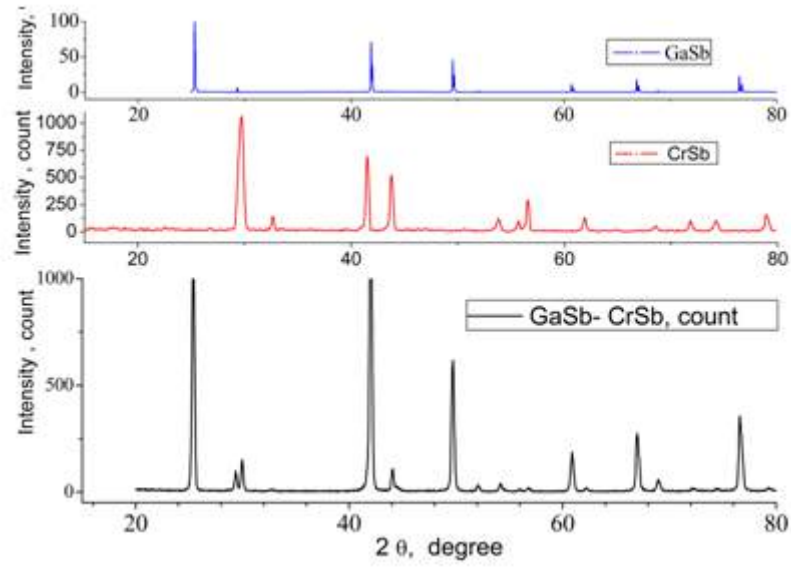


Fig. 1. Comparative diffraction patterns of GaSb and CrSb compounds and GaSb-CrSb eutectic composite.

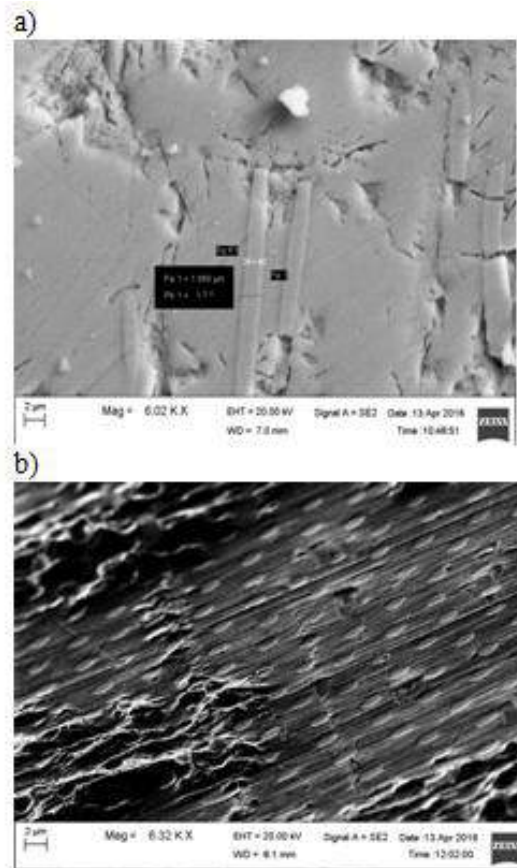


Fig 2. SEM micrographs of GaSb-CrSb showing cross sections of the samples along the (a) longitudinal and (b) lateral directions of the CrSb phase.

THERMAL AND ELECTRICAL PROPERTIES OF GaSb-CrSb EUTECTIC COMPOSITE

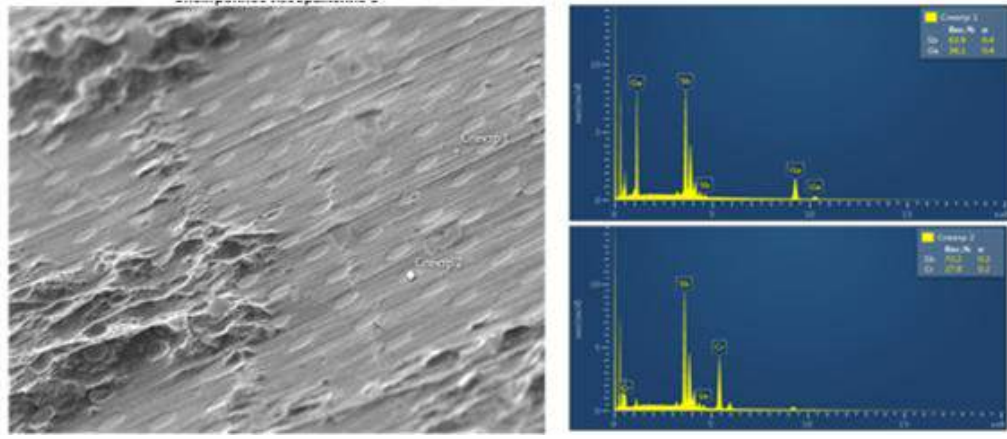


Fig. 3. X-ray spectra of GaSb–CrSb obtained with SEM–EDX from the needle and matrix phases along the lateral directions of the specimens

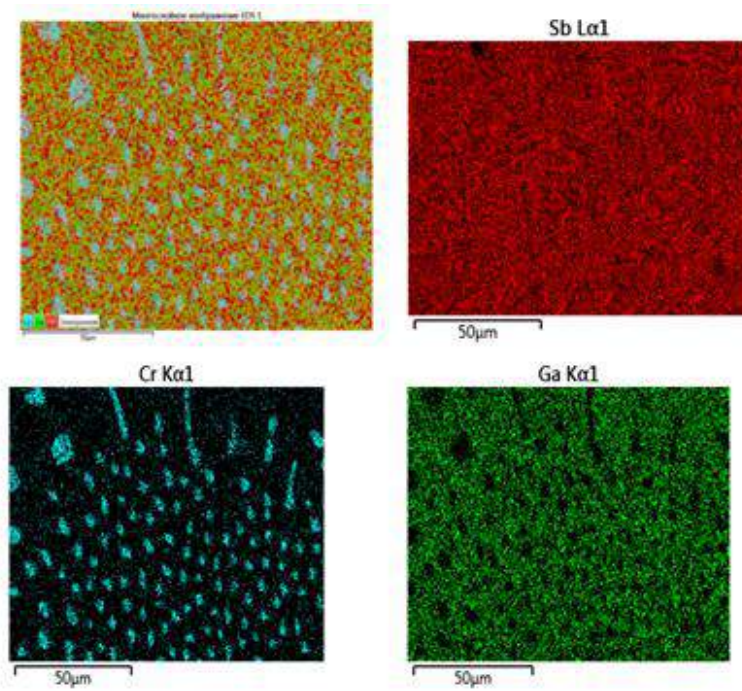


Fig.4. Element map of the GaSb–CrSb composite

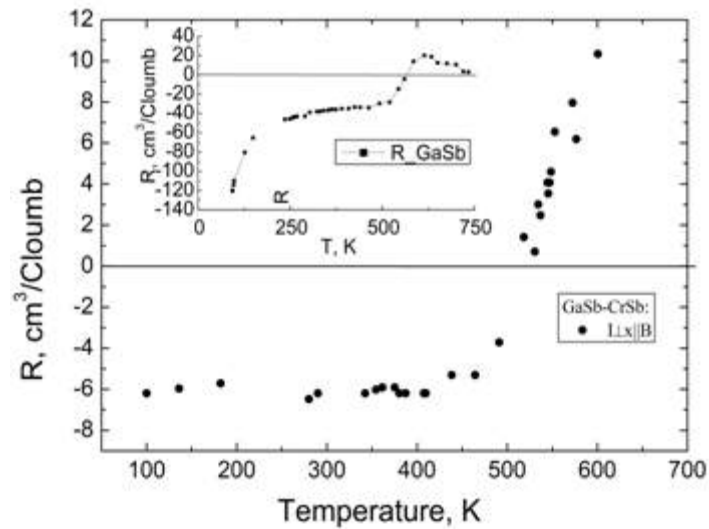


Fig.5. Temperature dependence of Hall coefficient for GaSb–CrSb composite. ($R(T)$ dependence for GaSb is shown in the insertion).

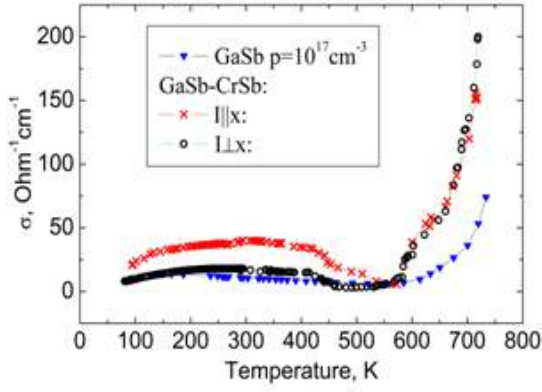


Fig.6. Temperature dependence of electric conductivity for GaSb and GaSb-CrSb composite.

As seen from Fig.6, due to short-circuiting action by needle-shaped inclusions, the electrical conductivity in the $I||x$ direction is significantly larger than that in the $I \perp x$ direction. The coefficient of conductivity anisotropy at 80 K is $\sigma_{||}/\sigma_{\perp} = 3.2$ and decreases with increasing temperature: $\sigma_{||}/\sigma_{\perp} = 3$ at 300 K. In the 400÷560 K temperature range the $\sigma(T)$ decreases in both directions, however, above 560 K, greatly increases and anisotropy completely disappears. The decrease of electrical conductivity is associated with the occurrence of a new flow of conduction electrons compensating of the hole conductivity. Above 560 K, the electron contribution to the conductivity and total mobility were increased. The deviation on the $\sigma(T)$ dependence observed in the 600÷650K temperature range is possibly due to the magnetic phase transition of the CrSb inclusions [8].

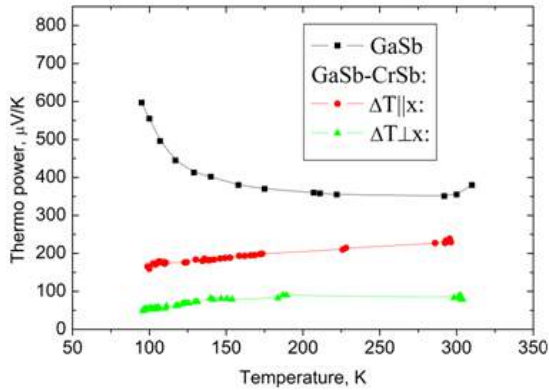


Fig.7. Temperature dependence of thermoelectric power for GaSb-CrSb composite.

Strong anisotropy is also observed in the temperature dependence of the thermoelectric power (Fig. 7). The short-circuiting of V_a potential by metallic inclusions in $\Delta T||x$ direction is caused by a decrease in the thermopower with anisotropy degree of $\alpha_{\perp}/\alpha_{||}=2.4$.

The temperature dependence of thermal conductivity $K(T)$ of GaSb-CrSb eutectic composite are presented on the fig. 8. Thermal conductivity up to 200K depends on temperature as $\sim T^{-0.8}$ (Fig.3). Two features are observed in the temperature dependence: the anisotropy in $K(T)$ in parallel and perpendicular directions of metallic

inclusions to the solidification front and additional thermal conductivity. At 80 K, anisotropy degree is 1.27, with temperature increasing it reduces and at room temperature disappears. The calculations have shown that free path length of the long-wavelength phonons is the same order as the transverse dimensions of metallic inclusions, which indicates the relationship of the observed anisotropy to the long-wavelength phonons scattering at the boundary inclusions.

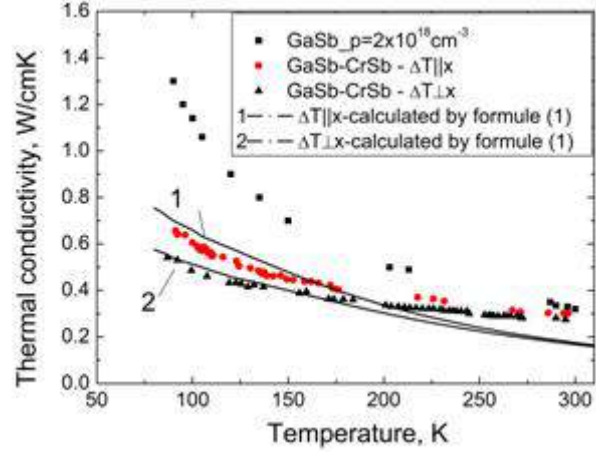


Fig.8. Thermal conductivity of GaSb and GaSb-CrSb composite, curves 1 and 2 are calculated from the formula (1).

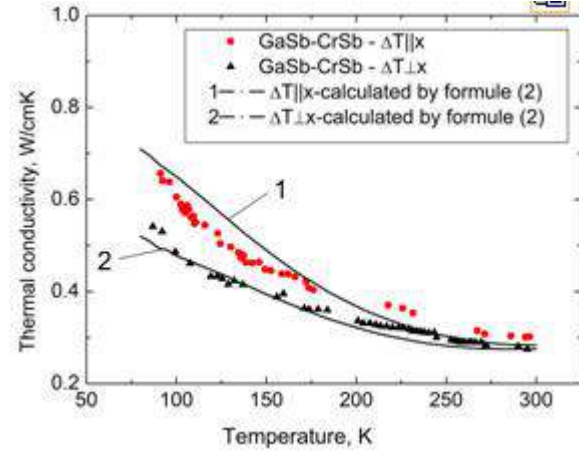


Fig.9. Thermal conductivity of GaSb and GaSb-CrSb composite, curves 1 and 2 are calculated from the formula (2).

The heat transfer mechanisms have been investigated in the framework of Callaway model. The total thermal conductivity of the composite is calculated taking into account contributions of the electron and phonon parts. Electronic thermal conductivity is calculated by the formula Wiedemann-Franz, and phonon thermal conductivity is for relaxation model of Callaway [10]:

$$K_f = \frac{k}{2\pi^2 v} \left(\frac{k}{\hbar} \right)^3 T^3 \int_0^{\theta/T} \frac{\tau_c z^4 e^z}{(e^z - 1)^2} dz ;$$

$$K_i = K_{el} + K_f , \quad (1)$$

here θ is the Debye temperature, $z = \frac{\hbar\omega}{k_0 T}$, ω is the phonon frequency, τ_c is the generalized relaxation time.

As can be seen from Fig.8, above 200K the calculated curve is below the experimental one due to the additional thermal conductivity which is 30% of the total at 300K. Most likely, in this region there are the other mechanisms of heat transfer. Such mechanisms can be magnon and photon thermal conductivity. However, calculations show that in this region, their parts in thermal conductivity are negligible. According to Koshino and Ando model [11] the resonance energy transfer can be the

dominant mechanism in thermal conductivity increasing. It is known that 3d- transition metal impurities may produce the deep and shallow impurity levels in the III-V group compounds [12]. When the excited electron from a deep local level in the band gap moves into the conduction band, other conduction electron returns to the shallow level. At thermal gradient, ionization energy is transferred to the cold edge of the sample. As seen from fig.6 electrical conductivity of GaSb-CrSb eutectic composite in the range of 80÷400K prevails over the extrinsic conductivity and in this region the resonance energy transfer is expressed as follows [11]:

$$K_R = 9.5 * 10^{-5} \left(\frac{m_0}{m^*} \right) \varepsilon_{\infty}^{\frac{1}{2}} n_d^{\frac{5}{4}} T^{\frac{5}{8}} (E_d^2 + 4E_d k_B T + 6k_B^2 T^2) e^{-E_d/k_B T} \quad K_2 = K_{el} + K_f + K_R \quad (2)$$

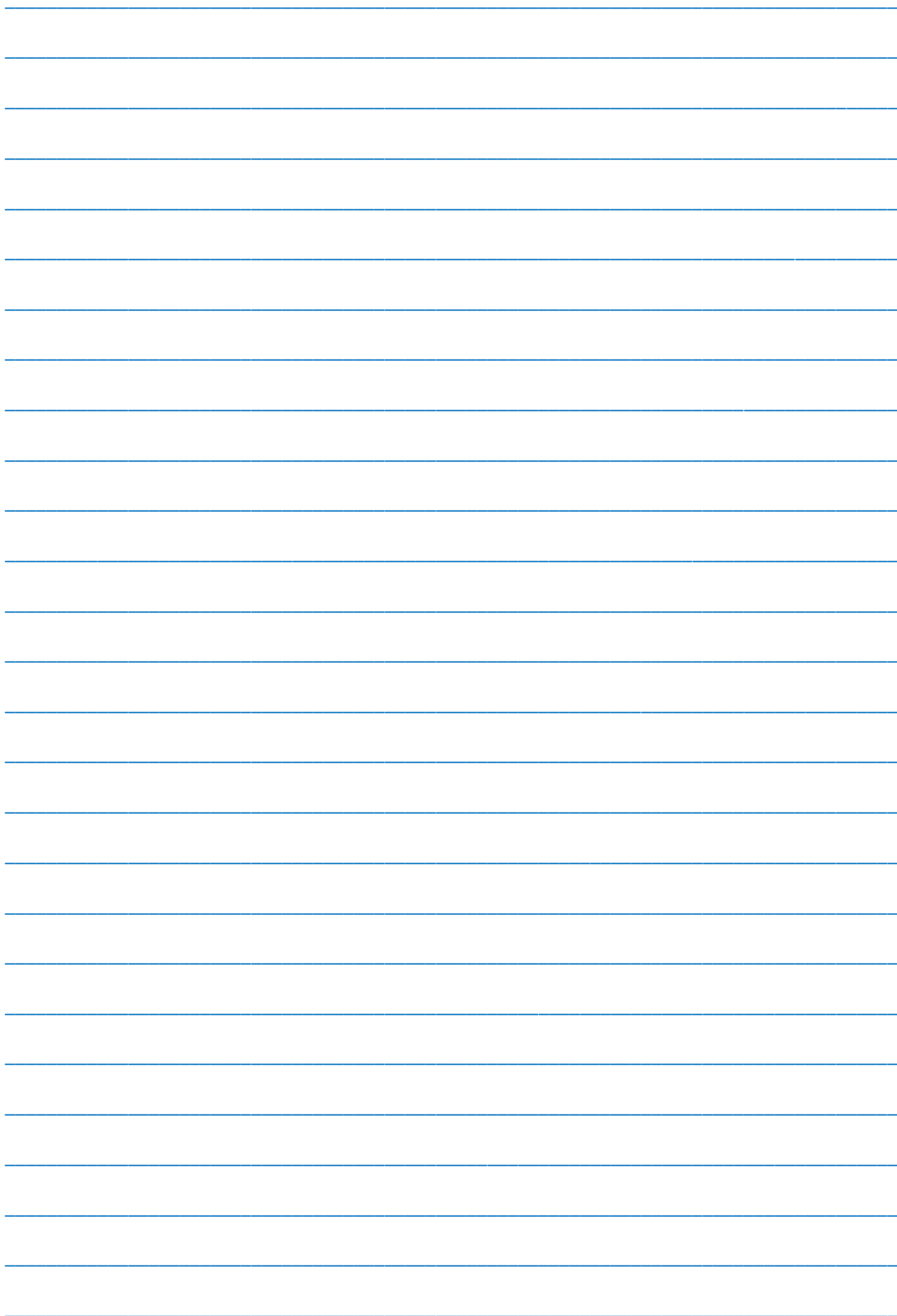
Here ε_{∞} is the dielectric constant, k_B is the Boltzmann constant, n_d is the local level concentration, E_d is the energy of the local level, m_0 is the mass of the electron, we have assumed $\varepsilon_{\infty}=16$ and $E_d=0.02\text{eV}$. The total thermal conductivity calculated by formula (2) well agrees with the experimental data (Fig. 9).

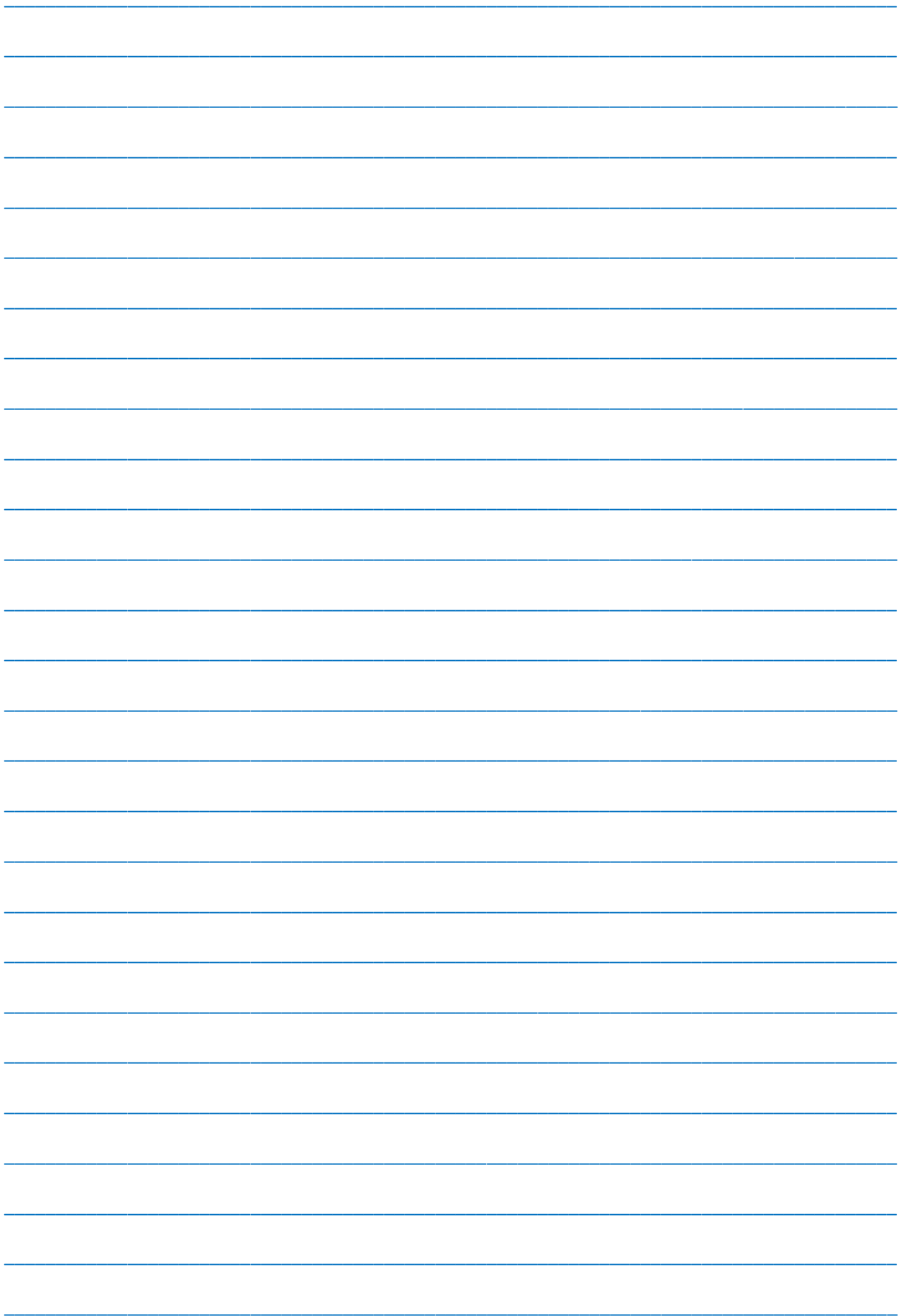
4. CONCLUSIONS

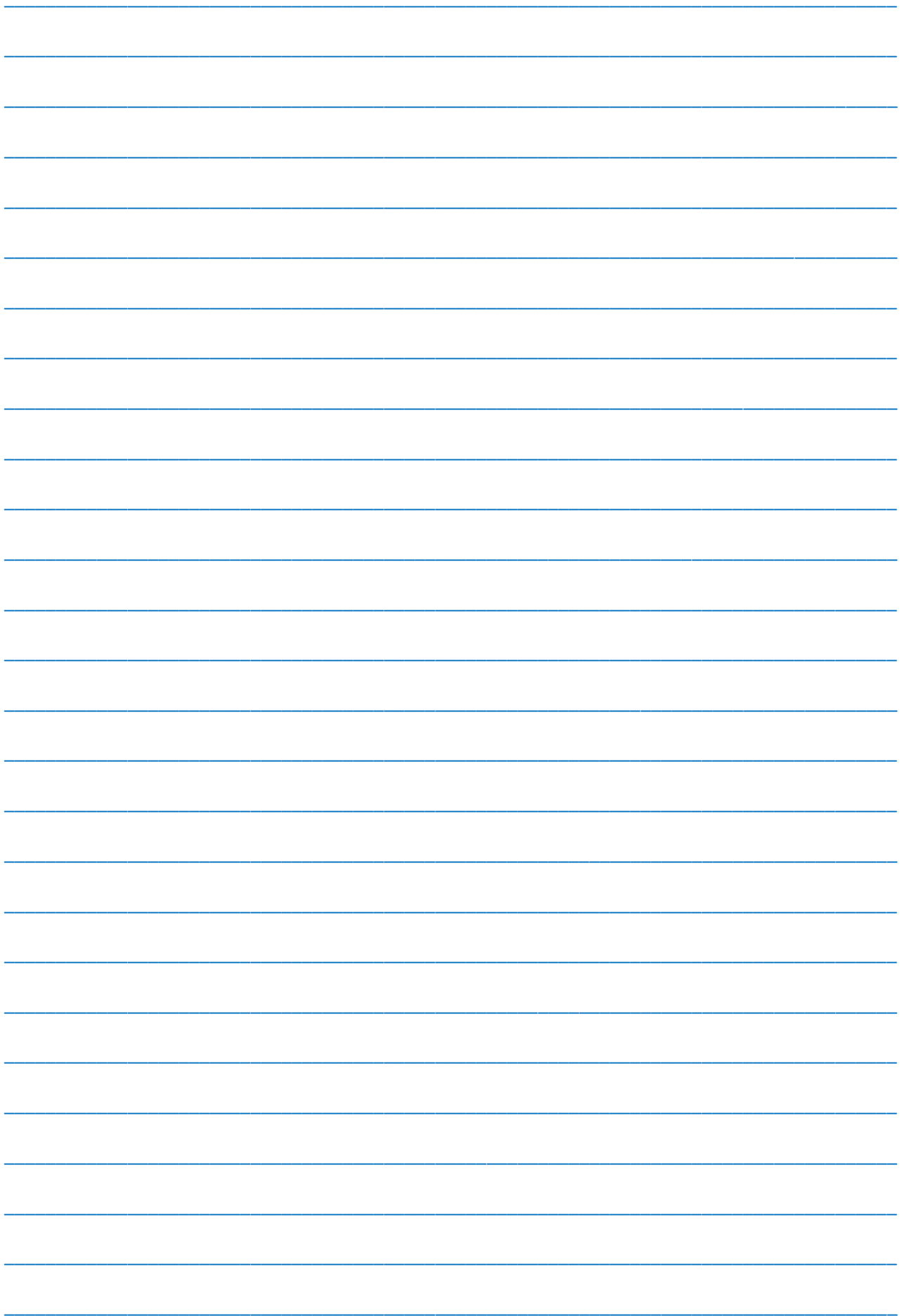
GaSb-CrSb eutectic alloys were prepared by the vertical Bridgman method. The two-phasesness of the GaSb-CrSb eutectic composite have been confirmed by the microstructure and morphology studies. The observed additional thermal conductivity in GaSb-CrSb is associated with the resonance energy transfer, while the anisotropy is associated with long-wavelength phonon scattering at the boundary inclusions.

- | | |
|---|---|
| <p>[1] <i>H. Weiss.</i> Structure and application of Galvanomagnetic devices, Pergamon Press, (1969).</p> <p>[2] <i>M.A. Sopovskaya, Y.S. Smetannikova.</i> FTP, (Semiconductors), 21, 7, 1242 (1987).</p> <p>[3] <i>R.N. Rahimov, A.A. Khalilova, D.H. Arasly, M.I. Aliyev, M. Tanoglu, L. Ozyuzer.</i> Sensors and Actuators A: Physical V 147, 436 (2008).</p> <p>[4] <i>S. Abe, T. Kaneko, M.Yoshida, K.Kamigaki.</i> Journal of the Physical Society of Japan. 53, 2703, (1984).</p> <p>[5] <i>S. Polesya, G. Kuhn, S. Mankovsky, H. Ebert, M. Regus, W. Bensch.</i> Structural and magnetic properties of CrSb compounds: NiAs structure., J Phys Condens Matter. (2012).</p> <p>[6] <i>M. Shirai.</i> J. Appl. Phys. 93, 6844 (2003).</p> <p>[7] <i>R.N. Rahimov, I.Kh. Mammadov, M.V. Kazimov, D.H. Arasly, A.A. Xəlilova.</i> Journal of Qafqaz University-Physics. 1, 166 (2013).</p> | <p>[8] <i>R.N. Rahimov, I.Kh. Mammadov, M.V. Kazimov, D.H. Arasly, A.A. Khalilova.</i> Structure and electrophysical properties of GaSb-CrSb eutectic composite, Moldavian Journal of the Physical Sciences, 14, 44 (2015).</p> <p>[9] <i>M.I. Aliyev, A.A. Khalilova, D.H. Arasly, R.N. Rahimov, M. Tanoglu, L. Ozyuzer.</i> J.Phys.D: Appl. Phys. 36, 2627 (2003).</p> <p>[10] <i>J. Callaway, H. Baeyer.</i> Effect of point-imperfections on lattice thermal conductivity. Phys. Rev., 120, 1149 (1960).</p> <p>[11] <i>S. Koshino, T. Ando.</i> J. Physical Society of Japan, 16, 1151 (1961).</p> <p>[12] <i>E.M. Omelyanovskiy, V.I. Fistul.</i> Impurity of Transition Metal in Semiconductors (in Russian) Moscow, Metallurgiya, 192 (1983).</p> |
|---|---|

Received: 24.02.2017







CONTENTS

1.	Gas discharge device based on the porous zeolite microstructure I.C. Koçum , U. Bunyatova, B.G. Salamov and M.M. Shirinov	3
2.	A microscopic theory of spin excitations in a cylindrical ferromagnetic nanotubes V.A. Tanriverdiyev, V.S. Tagiyev	8
3.	Superionic conduction in tlgase_2 crystal induced by γ -irradiation R.M. Sardarli, N.A. Aliyeva, F.T. Salmanov, A.P. Abdullayev, M.Y. Yusifov, A.A. Orudjeva	14
4.	Current oscillations in semiconductors with deep traps in strong electric and magnetic fields E.R. Gasanov, A.V. Islamzade, R.A. Gasanova	18
5.	Attractors in nano-structured layered crystals A.Sh. Kakhramanov, S.B. Bagirov	23
6.	Higgs boson production in neutrino-elektron scattering S. K. Abdullayev, M.S. Gojayev	27
7.	Mathematical modelling of the electron structure of SiO_2 nanoparticle A.G. Gasanov, A.A. Bayramov, E.G. Hashimov	34
8.	Thermal and electrical properties of Gasb-Crsb eutectic composite M.V. Kazimov	39



www.physics.gov.az